

1 **Development of the DO<sub>3</sub>SE-crop model to assess ozone effects on crop phenology,**  
2 **biomass and yield.**

3 Pritha Pande<sup>1</sup>; Sam Bland<sup>1</sup>; Nathan Booth <sup>2</sup>; Jo Cook<sup>2</sup>; Zhaozhong Feng<sup>3</sup>; Lisa Emberson<sup>2</sup>.

4 <sup>1</sup> Stockholm Environment Institute at York, Environment & Geography Dept., University of  
5 York, YO10 5DD, UK

6 <sup>2</sup> Environment & Geography Dept., University of York, YO10 5DD, UK

7 <sup>3</sup> Key Laboratory of Agrometeorology of Jiangsu Province, School of Ecology and Applied  
8 Meteorology, Nanjing University of Information Science & Technology, Nanjing, China.

9 Correspondence to: Pritha Pande (pritha.pande@york.ac.uk)

10 **Abstract**

11 A substantial body of empirical evidence exists to suggest that elevated O<sub>3</sub> levels are causing  
12 significant impacts on wheat yields at sites representative of highly productive arable regions around  
13 the World. Here we extend the DO<sub>3</sub>SE model (designed to estimate total- and stomatal-O<sub>3</sub>  
14 deposition for risk assessment) to incorporate a coupled  $A_{net}$ - $g_{sto}$  model to estimate O<sub>3</sub> uptake, an O<sub>3</sub>  
15 damage module (that impacts instantaneous  $A_{net}$  and the timing and rate of senescence), and a crop  
16 phenology, carbon allocation, and growth model based on the JULES-Crop model. The model  
17 structure allows scaling from the leaf to the canopy to allow for multiple leaf populations and  
18 canopy layers. The DO<sub>3</sub>SE-crop model is calibrated and parametrised using O<sub>3</sub> fumigation data from  
19 Xiaoji, China, for the year 2008 and for an O<sub>3</sub> tolerant and sensitive cultivar. The calibrated model  
20 was tested on data for different years (2007 and 2009) and for two additional cultivars and was  
21 found to simulate key physiological variables, crop development, and yield with a good level of  
22 accuracy. The DO<sub>3</sub>SE-crop model simulated the phenological stages of crop development under  
23 ambient and elevated O<sub>3</sub> treatments for the test datasets with an R<sup>2</sup> of 0.95 and an RMSE of 2.5  
24 days. The DO<sub>3</sub>SE-crop model was also able to simulate O<sub>3</sub>-induced yield losses of ~11-19 % compared  
25 to observed yield losses of 12-34 %, with an R<sup>2</sup> of 0.68 (n=20) and an RMSE of 76 g/m<sup>2</sup>. Additionally,  
26 our results indicate that the variance in yield reduction is primarily attributed to the premature  
27 decrease in carbon assimilation to the grains caused by accelerated leaf senescence, which is  
28 brought forward by 3-5 days under elevated O<sub>3</sub> treatments.

## 29 Introduction

30 Ground-level ozone ( $O_3$ ) is considered the most critical air pollutant causing global damage to  
31 agricultural crops. Elevated  $O_3$  concentrations are particularly problematic in Asia, where decades of  
32 rapid economic growth, industrialisation, and urbanisation have seen sharp rises in pollutant  
33 emissions associated with burning fossil fuels (Lin et al., 2017) causing substantial  $O_3$ -induced crop  
34 yield losses across the region (Feng et al., 2022). At the same time, climate change is considered a  
35 substantial threat to arable productivity through changes in average and extreme temperature and  
36 precipitation profiles across the region (IPCC, 2021). Reductions in precipitation are considered  
37 responsible for poor harvests in recent years (Liu et al., 2010), and rising temperatures that reduce  
38 the length of the crop growing season are thought to have caused losses in crop yield (Malhi et al.,  
39 2021). There is now substantial evidence showing that stresses from  $O_3$  pollution and climate  
40 variability interact, causing either additive, synergistic, or antagonistic responses in crop  
41 development, growth, and yield (Sillmann et al., 2021). The threat posed by these stresses is a  
42 particular cause for concern in Asia since the continent contributes approximately 43% of the global  
43 wheat production, with China contributing the highest production levels at 17% of the global wheat  
44 supply (Feng et al., 2021).  $O_3$  levels are rising substantially in important wheat-growing areas in  
45 China such as the North China Plain and the Yangtze River Delta (Li et al., 2020; Zhang et al., 2023).  
46 Concern over  $O_3$  impacts led to the implementation in 2013 of a range of policies to try to reduce  $O_3$   
47 precursor emissions across China. These included a comprehensive management plan to control  
48 volatile organic compounds (VOCs) from key industries, an atmospheric pollution prevention and  
49 control law of the People's Republic of China and, a 2020 VOCs Management Plan (Li et al., 2021). As  
50 a result, nitrogen oxide ( $NO_x$ ) emissions, an important  $O_3$  precursor, have decreased by 21% from  
51 2013 to 2017 (Li et al., 2021). By contrast, VOCs have only slightly decreased by 2% over the same  
52 period. Since China has a VOC limited  $O_3$  regime, the reductions in  $NO_x$  lead to rather insignificant  
53 changes in  $O_3$  concentration (Li et al., 2021) though evidence suggests that reductions in  $O_3$  may be  
54 higher in rural than urban areas (Lee et al., 2020). This implies future policies to tackle ground level  
55  $O_3$  pollution in China need to increase their focus on reducing VOCs along with  $NO_x$  (Lee et al., 2020)  
56 and also emphasise the importance of being able to make assessments of  $O_3$  damage to key  
57 receptors such as staple crops.

58 At present, methods to assess the risk to crop productivity from changes in  $O_3$  and climate variables  
59 use a variety of different  $O_3$  risk assessment methods (Ronan et al., 2020) and crop models as  
60 discussed in depth in Emberson et al. (2018). In the past,  $O_3$  risk assessment methods relied heavily  
61 on dose-response relationships, empirically derived relationships that assess changes in a response  
62 variable (most commonly yield) against an  $O_3$  exposure metric (concentration or, more recently, flux-  
63 based indices) (Pleijel et al., 2022). By contrast, methods to assess the impact of climate variables  
64 (most commonly changes in temperature, precipitation and  $CO_2$  concentration) tend to use crop  
65 models since these allow the integration of the combined effect of a number of different variables  
66 acting simultaneously to affect crop development, growth and yield (Schauberger et al., 2019). A  
67 new generation of crop models that include  $O_3$  damage are now being developed and applied and  
68 have the potential to estimate the combined effect of  $O_3$  and climate variables on crop  
69 development, biomass and yield. Such models can arguably be classified into two types of crop  
70 model. Firstly, those that rely on  $O_3$  metrics (e.g. AOT40 or M7) to modify crop growth determined  
71 by radiation use efficiency (Guarin et al., 2019; 2024) or evapotranspiration (Droustas et al., 2020).  
72 Secondly, those that estimate stomatal  $O_3$  uptake to modify crop growth determined by  
73 photosynthesis and subsequent carbon assimilation (Tao et al., 2017; Schauburger et al., 2019;  
74 Nguyen et al., 2024). The  $DO_3SE$ -Crop model falls into the latter category of photosynthetic-based  
75 crop models and was developed to bridge the gap between  $O_3$  risk assessment modelling methods  
76 and crop models.

77 The  $DO_3SE$  model is an  $O_3$  deposition model that can be embedded within atmospheric chemistry  
78 transport models (e.g. Simpson et al., 2012) and uses either a multiplicative or coupled  $A_{net}-g_{sto}$

79 model to estimate stomatal O<sub>3</sub> flux (Pande et al., 2024). Accumulated stomatal O<sub>3</sub> flux has been  
80 successfully used as a damage metric (PODy - Phytotoxic Ozone Dose over a threshold y (LRTAP,  
81 2017)) to predict O<sub>3</sub>-induced yield loss (Pande et al., 2024). The ability of the DO<sub>3</sub>SE model to  
82 simulate  $A_{net}$ , and the inclusion of a process-based O<sub>3</sub> damage module for both instantaneous  $A_{net}$   
83 and early and enhanced senescence (after Ewert and Porter (2000)) lends itself to the development  
84 of the DO<sub>3</sub>SE model as a process-based crop model. The inclusion of resistance algorithms that can  
85 assess the transport of O<sub>3</sub> concentrations from a reference height above a canopy down to the  
86 canopy top, means the model can be embedded within existing atmospheric chemistry transport  
87 schemes and hence applied for regional or global scale O<sub>3</sub> risk assessment whilst also modelling O<sub>3</sub>  
88 deposition. A comparison of the coupled stomatal  $A_{net}$ - $g_{sto}$  model with the multiplicative  $g_{sto}$  model  
89 within the DO<sub>3</sub>SE framework has been made in Pande et al. (2024) and showed that the  $A_{net}$ - $g_{sto}$   
90 model performed equally well, if not better, when used to develop O<sub>3</sub> dose-response relationships  
91 for European wheat. This provides evidence of the suitability of the new photosynthetic based  $g_{sto}$   
92 model in DO<sub>3</sub>SE.

93  
94 In this study, we describe the development of a new DO<sub>3</sub>SE-Crop model which builds on the  
95 modified stomatal deposition component of the DO<sub>3</sub>SE model (Pande et al. 2024) so that both CO<sub>2</sub>  
96 uptake for carbon assimilation as well as O<sub>3</sub> uptake via the stomata can be modelled consistently.  
97 Further, we have incorporated the UK JULES crop model (Osborne et al., 2015) to allocate  
98 assimilated carbon to plant components (roots, leaves, stems and harvest organs) according to crop  
99 development stage. We also take account of the modifying effect of O<sub>3</sub> on instantaneous  $A_{net}$  as well  
100 as accumulated  $A_{net}$  via O<sub>3</sub> effects on the onset and rate of leaf senescence and timing of crop  
101 maturity through incorporation of algorithms developed by Ewert and Porter (2000). The UK JULES  
102 crop model is used since this is the UK land surface exchange scheme in the UK Earth System Model  
103 (UKESM) (Osborne et al., 2015) which has recently been developed to include exchange and impact  
104 of trace gases (including O<sub>3</sub>) along with other biogeochemical cycling between the atmosphere and  
105 the land surface (Leung et al., 2020). This would in the future allow comparison of the UK JULES Crop  
106 model, which uses O<sub>3</sub> mechanisms that modify instantaneous  $A_{net}$  to mimic changes in yield  
107 consistent with flux-response relationships (Sitch et al., 2007), with the alternative O<sub>3</sub> damage  
108 mechanisms used within DO<sub>3</sub>SE-crop.

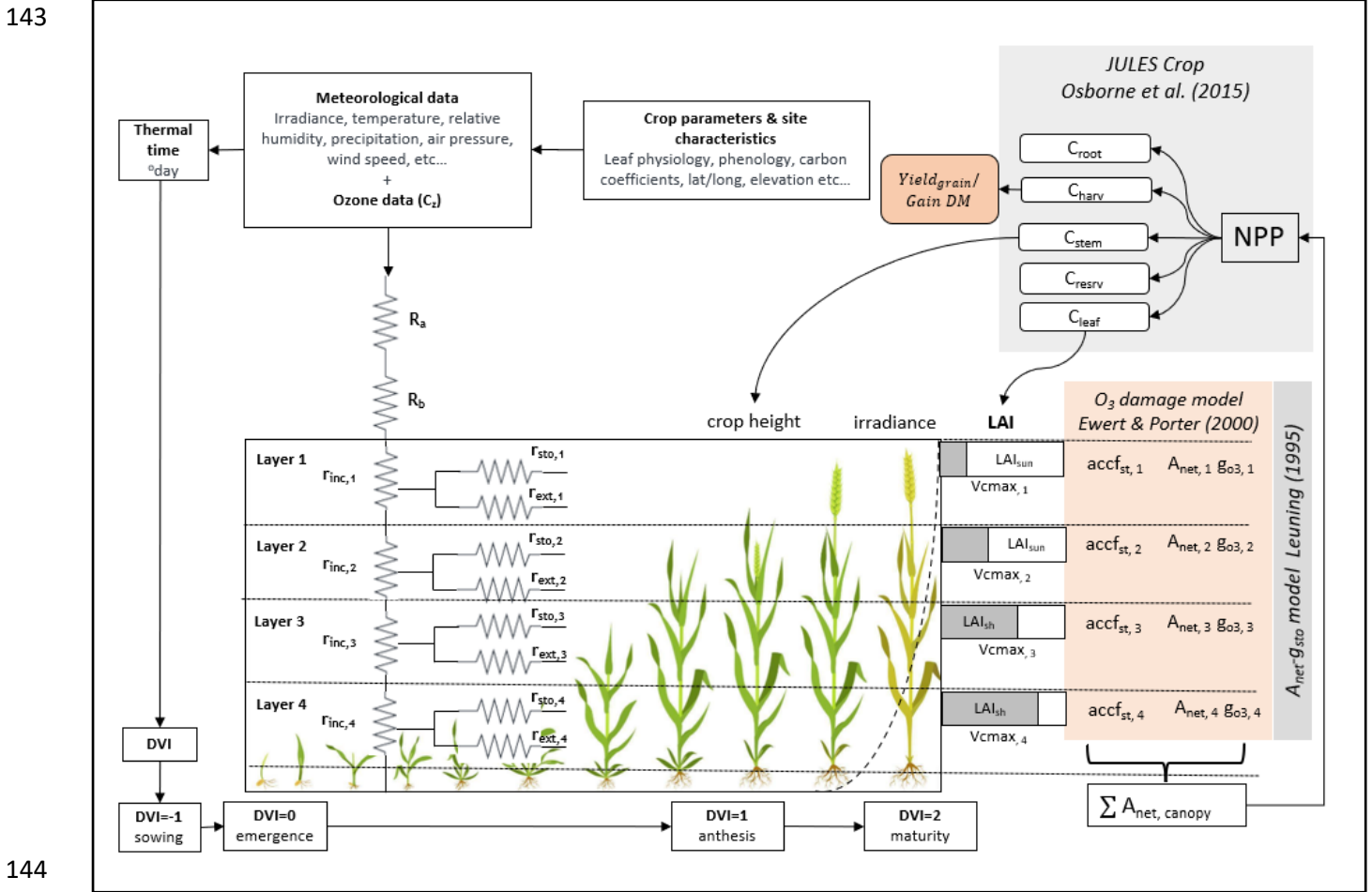
109 Here, we calibrate and evaluate the DO<sub>3</sub>SE-crop model using an experimental FACE dataset collected  
110 in Xiaoji, China. This allows us to investigate the ability of the model to simulate O<sub>3</sub> damage for a  
111 ~~comparable agro-ecological region global-region~~ where crop productivity is severely threatened by  
112 both O<sub>3</sub> pollution and climate change. The key objectives of the paper are to assess the ability of  
113 DO<sub>3</sub>SE-Crop to simulate i). key phenological stages, ii) the relationship between leaf-level  
114 physiological variables and within canopy O<sub>3</sub> concentrations, iii) C allocation to different parts of the  
115 crop and iv) O<sub>3</sub> induced yield losses for tolerant and sensitive cultivars.

## 116 Methods

### 117 1. DO<sub>3</sub>SE-Crop Model

118 Here we describe the development of the DO<sub>3</sub>SE-Crop model (version 4 (V4.39.19)) for wheat  
119 (*Triticum aestivum*) which is widely considered to be one of the most sensitive staple crops to O<sub>3</sub>  
120 (Feng et al., 2018). The key components of DO<sub>3</sub>SE Crop are illustrated in Fig.1. The model integrates  
121 meteorological data, crop parameters, and site characteristics to simulate the impact of O<sub>3</sub> on crop  
122 yield. Model inputs are irradiance, temperature, relative humidity, precipitation, air pressure, wind  
123 speed, and O<sub>3</sub> concentration at a reference height ( $C_z$ ) to calculate atmospheric resistances ( $R_a$ ) and  
124 boundary layer resistances ( $R_b$ ) for O<sub>3</sub> deposition to the crop canopy. It further incorporates crop-  
125 specific parameters related to leaf physiology, phenology and carbon coefficients, alongside site-  
126 specific data (latitude, longitude and elevation) to simulate crop growth at stages from sowing to  
127 maturity, denoted by the Development Vegetative Index (DVI). The canopy is divided into four  
128 vertical layers, each characterised by sunlit ( $LAI_{sun}$ ) and shaded ( $LAI_{sh}$ ) leaf area index, which  
129 influence the photosynthetic capacity ( $V_{cmax}$ ) and O<sub>3</sub> uptake in each layer. The model accounts for  
130 in-canopy resistance ( $r_{inc}$ ) and external resistance ( $r_{ext}$ ) in each layer, affecting the O<sub>3</sub> flux ( $accf_{st}$ )  
131 and its impact on net photosynthesis ( $A_{net}$ ) and stomatal conductance ( $g_{o_3}$ ). The  
132  $A_{net}g_{sto}$  relationship is modeled using the Leuning model (1995). Damage from O<sub>3</sub> is estimated after  
133 Ewert & Porter (2000) for different canopy layers, which are aggregated to give the overall O<sub>3</sub> impact  
134 on canopy  $A_{net}$  which is integrated according to the JULES Crop model (Osborne et al., 2015), which  
135 uses the daily accumulated canopy  $A_{net}$  to calculate the net primary productivity (NPP). The NPP is  
136 then distributed as carbon to various parts of the crop (roots ( $C_{root}$ ), stems ( $C_{stem}$ ), leaves ( $C_{leaf}$ ),  
137 harvestable organs ( $C_{harv}$ )). The  $C_{harv}$  provides the yield and grain dry matter;  $C_{leaf}$  the LAI and  
138  $C_{stem}$  the crop height. [The DO<sub>3</sub>SE-Crop model requires hourly input meteorological and O<sub>3</sub>  
139 concentration data which is used to produce output on either an hourly \(i.e. leaf physiology and  
140 short-term O<sub>3</sub> damage variables\) or daily \(i.e. phenology, soil moisture, long-term O<sub>3</sub> damage, C  
141 allocation, biomass and yield variables\) time step.](#)

142 Fig. 1 Schematic of the DO<sub>3</sub>SE-Crop model.



### 145 1.1 DO<sub>3</sub>SE-Crop Phenology

146 The DO<sub>3</sub>SE-Crop model uses thermal time to define the rate of crop development in relation to the  
 147 timing of three key developmental stages,  $TT_{emr}$  (the period from sowing to emergence),  $TT_{veg}$  (the  
 148 period of emergence to start of grain filling) and  $TT_{rep}$  (the period from the start of grain filling to  
 149 maturity) based on the method of Osborne et al. (2015). Thermal time is calculated by accumulating  
 150 an effective temperature ( $T_{eff}$ ) using base ( $T_b$ ), optimum ( $T_o$ ) and maximum ( $T_m$ ) cardinal  
 151 temperatures as shown in eq. [1].

$$152 \quad T_{eff} = \begin{cases} 0 & \text{for } T_{air} < T_b \\ T_{air} - T_b & \text{for } T_b \leq T_{air} \leq T_o \\ (T_o - T_b) \left(1 - \frac{T_{air} - T_o}{T_m - T_o}\right) & \text{for } T_o < T_{air} < T_m \\ 0 & \text{for } T_{air} \geq T_m \end{cases} \quad [1]$$

153 Where,  $T_{air}$  is the surface air temperature in °C,  $T_{eff}$  is at a maximum when  $T_{air} = T_o$ , this point  
 154 denotes the highest developmental rate.  $T_{eff}$  declines as the temperature falls or rises above  $T_o$ ,  
 155 with a linear decrease in crop development.  $T_{eff}$  is zero, i.e. no development, when  $T_{air}$  falls below  
 156 or rises above  $T_b$  and  $T_m$  respectively i.e.  $T_m \leq T_{air} < T_b$ . During the sowing to emergence phase,

157 development is dependent on  $T_b$ , whereas during the vegetative and reproductive phase,  
 158 development depends on  $T_m$  or  $T_o$ .

159 Winter wheat requires vernalisation (a period of exposure to low temperature during germination to  
 160 accelerate flowering). Vernalisation alters the length of  $TT_{veg}$  and hence flowering initiation, with  
 161 subsequent effects on later growth stages such as heading. Vernalisation occurs when the minimum  
 162 ( $VT_{min}$ ) and maximum ( $VT_{max}$ ) daily temperature is less than 15°C and 30°C respectively (Zheng et  
 163 al., 2015). Accumulated vernalised days ( $V_{dd}$ ) are calculated as the sum of vernalised and  
 164 devernalised days from emergence to the start of anthesis (Zheng et al., 2015) as shown in eq. [2].

$$165 \quad V_{dd} = \sum(V - V_d), \text{ where} \quad [2]$$

$$166 \quad V = \left(1.4 - 0.778 \times T_{air}, 0.5 + 13.44 \frac{T_{air}}{(T_{max} - T_{min} + 3)^2}\right) \quad \text{for } VT_{max} < 30^\circ\text{C and } VT_{min} < 15^\circ\text{C}$$

$$167 \quad V_d = (\min(0.5(T_{max} - 30), V_{prev})) \quad \text{for } VT_{max} > 30^\circ\text{C and } V_{dd} < 10 \text{ days}$$

168 The vernalisation factor ( $VF$ ) decreases from 1 to 0 as ( $V_{dd}$ ) increases.  $VF$  depends on a cultivar-  
 169 specific vernalisation coefficient ( $PIV$ ) as described by eq. [3].

$$170 \quad VF = 1 - (0.0054545 \times PIV + 0.0003) * (50 - V_{dd}) \quad [3]$$

171 Photoperiod ( $PP$ ) or day length also affects the occurrence and timing of the flowering stage and is  
 172 calculated according to latitude using standard solar geometry to estimate daylength (Jones, 1992).  
 173 The photoperiod factor ( $PF$ ) represents the sensitivity to  $PP$  which decreases from 1 to 0 as the  
 174 photoperiod shortens and is estimated according to a cultivar-specific photoperiod coefficient ( $PID$ )  
 175 after Tao et al. (2012) as described in eq. [4].

$$176 \quad PF = 1 - \left[\left(\frac{PID}{10000}\right) \times (20 - PP)^2\right] \quad [4]$$

177 Crop development is related to the development index ( $DVI$ ) after Osborne et al. (2015) which takes  
 178 values of -1 upon sowing, 0 on emergence, 1 at anthesis and 2 at crop maturity. The DO<sub>3</sub>SE-Crop  
 179 model  $DVI$  equations have been modified from Osborne et al. (2015) to take account of the  
 180 photoperiod and vernalisation for winter wheat (see eq. [5]); for spring wheat these factors are  
 181 omitted.

$$182 \quad -1 \leq DVI < 0 \quad \text{for } TT_{eff} < TT_{emr}$$

$$183 \quad 0 \leq DVI < 1 \quad \text{for } TT_{emr} \leq TT_{eff} \times VF \times PF < TT_{veg} \quad [5]$$

$$184 \quad 1 \leq DVI \leq 2 \quad \text{for } TT_{veg} \leq TT_{eff} \leq TT_{rep}$$

185 DO<sub>3</sub>SE-Crop allows for any number of representative leaf populations ( $pop$ ) and canopy layers ( $n$ )  
 186 to be defined over the course of the crop growing season [by dividing leaf populations as they](#)  
 187 [emerge evenly across the canopy layers defined by LAI](#). In this study, we used a single leaf  
 188 population and 4 canopy layers (i.e.  $pop = 1$ ;  $n = 4$ ) for simplicity. The crop sowing is assumed to  
 189 be at  $DVI = -1$  (start of  $TT_{emr}$ ) and emergence at  $DVI = 0$  (start of  $TT_{veg}$ ). The flag leaf is assumed to  
 190 develop at  $DVI=1$ , at the commencement of  $TT_{rep}$ , marking the initiation of anthesis ( $A_{start}$ ,  
 191 flowering) and flag leaf emergence, which typically occurs 4-5 days prior to the onset of anthesis and  
 192 is further divided into expanding and senescing leaf periods (i.e.  $tl_{ep}$  and  $tl_{se}$ ) with a default ratio of  
 193 0.67 to 0.33 for each of these periods. Maturity is assumed at  $DVI = 2$ , at the end of  $TT_{rep}$ . The model  
 194 allows estimation of the  $PODy$  metric by accumulating stomatal O<sub>3</sub> flux from the start of anthesis to  
 195 maturity. The total canopy-leaf life span ( $TT_{leaf}$ ) of the crop is distributed over the  $DVI$  between 0

196 and 2. The total lifespan ( $T_l$ ) covers the full period from sowing to maturity, corresponding to DVI  
 197 between -1 to 2. The relationship between these different variables is described in Fig. 2.

## 198 1.2 DO<sub>3</sub>SE-Crop leaf-level physiology

199 Key leaf-level physiological variables of the DO<sub>3</sub>SE-Crop model are  $A_{net}$  and  $g_{sto}$ . Net photosynthesis  
 200 is simulated using the biochemical photosynthesis-based model initially developed by (Farquhar et  
 201 al., 1980) and since modified by Sharkey et al. (2007). The coupled  $A_{net}g_{sto}$  model of Leuning (1995)  
 202 is used to estimate  $g_{sto}$  from  $A_{net}$  which means that  $g_{sto}$  is regulated by the demand of CO<sub>2</sub> for  
 203  $A_{net}$  on consideration of environmental conditions and crop physiology. Ozone stress, causing both  
 204 instantaneous effects on  $A_{net}$  and long-term effects on  $A_{net}$  via leaf senescence is simulated based  
 205 on algorithms developed by Ewert and Porter (2000).

### 206 1.2.1 Leaf net photosynthesis ( $A_{net}$ )

207 The  $A_{net}$  model assumes that photosynthesis is constrained depending on prevailing environmental  
 208 conditions according to three main mechanisms: Rubisco activity ( $A_c$ ); ribulose-1,5-bisphosphate  
 209 (RuBP) regeneration, which is constrained by the speed of electron transport ( $A_j$ ); and the low rate  
 210 of transfer of photosynthetic products (most frequently triose phosphate consumption) ( $A_p$ )  
 211 (Sharkey et al., 2007) and by soil water stress ( $f_{PAW}$ ); the algorithm for  $A_c$  which is based on Medlyn  
 212 et al. (2002) and modified in DO<sub>3</sub>SE-crop to include the O<sub>3</sub> damage functions is given in eq. [6].

$$213 \quad A_c = V_{cmax} \times f_{PAW} \times \frac{(C_i - \Gamma^*) \times f_{O_{3,s}}(d) \times f_{LS}}{C_i + K_c \left(1 + \frac{O_i}{K_o}\right)} \quad [6]$$

214 where  $V_{cmax}$  ( $\mu\text{mol CO}_2 \text{ m}^{-2}\text{s}^{-1}$ ) is the maximum carboxylation capacity at 25°C,  $C_i$  ( $\mu\text{mol mol}^{-1}$ ) and  
 215  $O_i$  ( $\text{mmol mol}^{-1}$ ) are the intercellular CO<sub>2</sub> and O<sub>2</sub> partial pressures;  $K_c$  ( $\mu\text{mol mol}^{-1}$ ) and  $K_o$  ( $\text{mmol}$   
 216  $\text{mol}^{-1}$ ) are the Rubisco Michaelis-Menten constants for CO<sub>2</sub> and O<sub>2</sub>;  $\Gamma^*$  ( $\mu\text{mol mol}^{-1}$ ) is the CO<sub>2</sub>  
 217 compensation point in the absence of respiration;  $f_{O_{3,s}}(d)$  is the factor that accounts for the  
 218 cumulative stomatal O<sub>3</sub> flux effect on  $V_{cmax}$  over the course of a day and;  $f_{LS}$  is the factor that  
 219 accounts for the cumulative stomatal O<sub>3</sub> flux effect over the course of a leaf life span on leaf  
 220 senescence. Section 1.2.1.1 gives a full description of the methods used to estimate O<sub>3</sub> damage. The  
 221  $f_{PAW}$  factor is calculated by eq. [7].

$$222 \quad f_{PAW} = 1 \quad \text{for } PAW_t \leq PAW \leq 100\%, \quad [7]$$

$$223 \quad f_{PAW} = 1 + \left\{ \frac{PAW / PAW_t}{PAW_t} \right\} \quad \text{for } PAW \leq PAW_t$$

224  $PAW$  is the amount of water in the soil (in % terms) which is available to the plant [estimated](#)  
 225 [according to the DO<sub>3</sub>SE models single soil layer bucket model \(Bueker et al., 2012\)](#). -At  $PAW=100\%$   
 226 the soil is at field capacity, at  $PAW=0\%$  the soil is at wilting point.  $PAW_t$  is the threshold  $PAW$ , above  
 227 which it is assumed there is no constraint on  $A_c$ , defined as 50% after LRTAP (2017). [Only once  \$PAW\$](#)   
 228 [<  \$PAW\_t\$  will soil water begin to limit  \$g\_{sto}\$  and hence stomatal O<sub>3</sub> flux.](#)

229 The constraint on photosynthesis due to the rate of electron transport  $A_j$  is described in eq. [8].

$$230 \quad A_j = J \times \frac{C_i - \Gamma^*}{a \times C_i + b \times \Gamma^*} \quad [8]$$

231 where  $J$  is the electron transport rate ( $\mu\text{mol CO}_2 \text{ m}^{-2}\text{s}^{-1}$ ), the parameters  $a$  and  $b$  denote the electron  
 232 requirements for the formation of NADPH and ATP respectively (Sharkey et al., 2007)

233 Finally, the photosynthesis limitation due to the low rate of transfer of photosynthetic products  $A_p$   
 234 ( $\mu\text{mol CO}_2 \text{ m}^{-2}\text{s}^{-1}$ ) is given in eq. [9].

$$235 \quad A_p = 0.5 \times V_{cmax} \quad [9]$$

236 The leaf net photosynthesis ( $A_{net}$ ) in  $\mu\text{mol CO}_2 \text{ m}^{-2}\text{s}^{-1}$  is calculated by eq. [10]

$$237 \quad A_{net} = (A_c, A_j, A_p) - R_d \quad [10]$$

238

239 Where leaf dark respiration ( $R_d$ ) in  $\mu\text{mol CO}_2 \text{ m}^{-2}\text{s}^{-1}$  is calculated as  $V_{cmax} \times R_{dcoeff}$  where  $R_{dcoeff}$   
 240 is the leaf dark respiration coefficient initially set equal to 0.015 after Clark et al. (2011), a value  
 241 provided for C3 grasses.

#### 242 1.2.1.1 Short- and long-term O<sub>3</sub> damage to $A_c$

243 The short-term impact of O<sub>3</sub> on  $A_c$  is calculated according to the  $f_{O_{3,s}}(d)$  factor (between 0 and 1)  
 244 which allows for an instantaneous effect of O<sub>3</sub> on photosynthesis when stomatal O<sub>3</sub> flux ( $f_{st}$ ), in  
 245  $\text{nmol O}_3 \text{ m}^{-2} \text{ s}^{-1}$  calculated as described later in section 1.2.3, overwhelms detoxification and repair  
 246 mechanisms (Betzberger et al., 2012; Feng et al., 2022), and is estimated following Ewert and  
 247 Porter (2000). Here,  $f_{O_{3,s}}(h)$  represents the relationship between  $f_{st}$  and a potential decrease in  $A_c$   
 248 calculated for every hour of the day by eq. [11].

$$249 \quad f_{O_{3,s}}(h) = 1 ; \quad \text{for } f_{st} \leq \frac{\gamma_1}{\gamma_2}$$

$$250 \quad f_{O_{3,s}}(h) = 1 + \gamma_1 - \gamma_2 \times f_{st} \quad \text{for } \frac{\gamma_1}{\gamma_2} < f_{st} < \frac{1+\gamma_1}{\gamma_2} \quad [11]$$

$$251 \quad f_{O_{3,s}}(h) = 0 ; \quad \text{for } f_{st} \geq \frac{1+\gamma_1}{\gamma_2}$$

252 where  $\gamma_1$  (dimensionless) and  $\gamma_2$  ( $\text{nmol O}_3 \text{ m}^{-2} \text{ s}^{-1}$ )<sup>-1</sup> are both short-term O<sub>3</sub> damage coefficients,  
 253 with  $\gamma_1$  representing the O<sub>3</sub> detoxification threshold below which no damage occurs to the  
 254 photosynthetic system and  $\gamma_2$  determines the effect of  $f_{st}$  on  $A_c$  once this detoxification threshold  
 255 is exceeded;  $f_{O_{3,s}}(d)$  and  $f_{O_{3,s}}(d - 1)$  (i.e.  $f_{O_{3,s}}(d)$  at the end of the previous day), are calculated  
 256 by eq. [12].

$$257 \quad f_{O_{3,s}}(d) = f_{O_{3,s}}(h) \times r_{O_{3,s}} ; \quad \text{for } PAR \leq 50 \text{ W m}^{-2}$$

$$258 \quad f_{O_{3,s}}(d) = f_{O_{3,s}}(h) \times f_{O_{3,s}}(d - 1) \quad \text{for } PAR > 50 \text{ W m}^{-2} \quad [12]$$

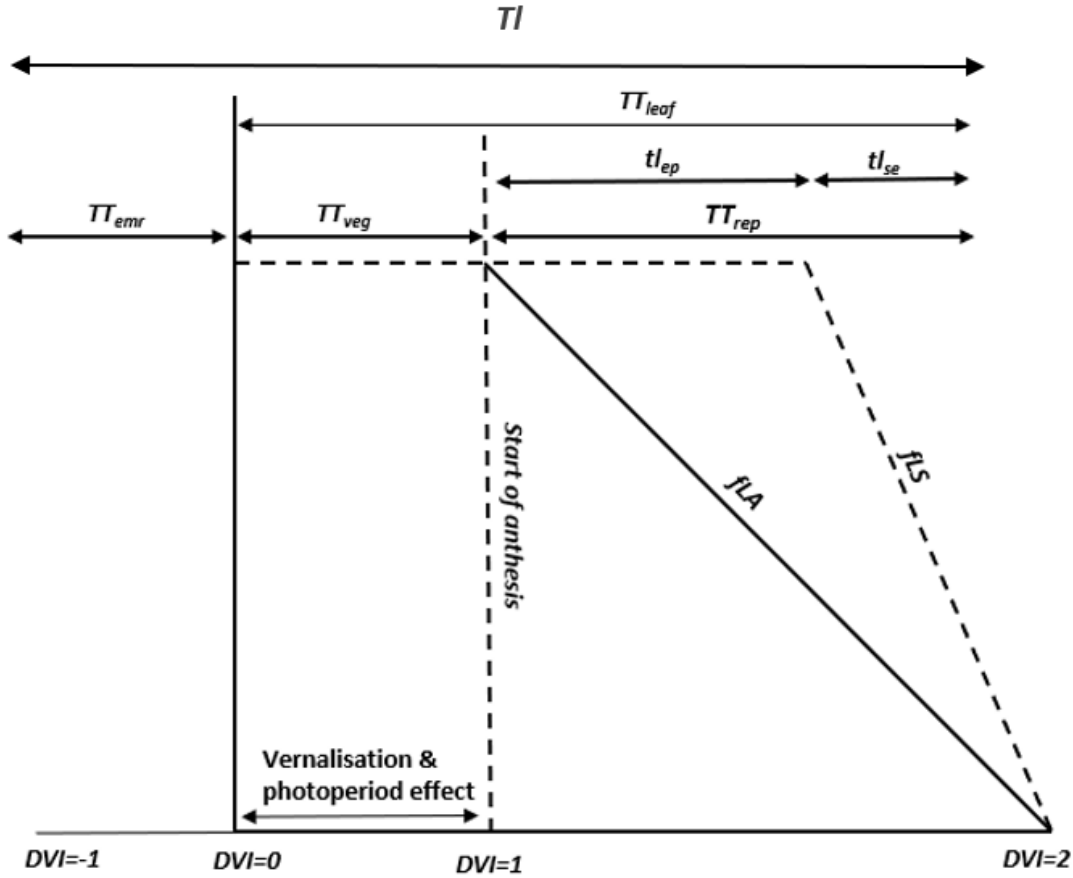
259 where  $r_{O_{3,s}}$  (dimensionless) represents incomplete recovery from O<sub>3</sub> overnight which depends on  
 260 leaf age according to eq. [13].

$$261 \quad r_{O_{3,s}} = f_{O_{3,s}}(d - 1) + (1 - f_{O_{3,s}}(d - 1)) \times f_{LA} \quad [13]$$

262 The long-term impact of O<sub>3</sub> on  $V_{cmax}$  represented by the  $f_{LS}$  term represents the longer-term  
 263 accumulation of stomatal O<sub>3</sub> flux ( $acc_{fst}$ ) causing degradation to the Rubisco enzyme which triggers  
 264 early and enhanced senescence of mature leaves (Gelang et al., 2000; Osborne et al., 2019). The  
 265  $acc_{fst}$  term is accumulated from 200°C days before anthesis until maturity to be consistent with the  
 266 LRTAP (2017) which defines this as the O<sub>3</sub> sensitive period for wheat. The simulation of  $f_{LS}$  (and  $f_{LA}$   
 267 used in the short-term O<sub>3</sub> effect) are related to thermal time defined periods over the course of a  
 268 leaf population life span  $TT_{leaf}$  as described in Fig. 2.



269 Fig 2. The division of thermal time defined periods ( $TT_{emr}$ ,  $TT_{veg}$ ,  $TT_{rep}$  and  $TT_{leaf}$  and the  
 270 relationship with  $f_{LA}$  and  $f_{LS}$ ) for the canopy, as represented in this study by a single leaf population.



271

272 The  $O_3$  effect on  $f_{LS}$  is first simulated by estimating a weighted accumulated  $f_{st}$  ( $fO3_l$ ) modified  
 273 from Ewert and Porter (2000) by eq. [14].

$$274 \quad fO3_l = 1 - \max(\min(\gamma3 \times (acc_{fst} - CLsO3), 1), 0) \quad [14]$$

275 where  $\gamma3$  determines the occurrence of senescence once a critical cumulative stomatal  $O_3$  flux  
 276  $CLsO3$  (in  $mmol/m^2$ ) has been exceeded. The rate of senescence is determined by  $\gamma4$ , which  
 277 determines the onset of senescence and  $\gamma5$  which determines maturity as described in eq. [15]

$$278 \quad tl_{epO3} = tl_{ep} \times (1 - ((1 - fO3_l) \times \gamma4))$$

$$279 \quad tl_{seO3} = tl_{se} \times (1 - ((1 - fO3_l) \times \gamma5)) + zc \quad [15]$$

$$280 \quad zc = tl_{ep} - tl_{epO3}$$

281 Where  $tl_{ep}$  is the thermal time accumulated by a leaf ( $LTT$ ) in  $^{\circ}C$  days between a fully expanded leaf  
 282 and the start of leaf senescence,  $tl_{epO3}$  is  $tl_{ep}$  with an  $O_3$  effect which may bring senescence earlier,  
 283  $tl_{se}$  is the  $LTT$  in  $^{\circ}C$  days between the onset of senescence and maturity and  $tl_{seO3}$  is  $tl_{se}$  with an  $O_3$   
 284 effect which may bring maturity earlier.  $f_{LS}$  is estimated by eq. [16].

$$285 \quad f_{LS} = 1; \quad \text{for } LTT \leq TT_{veg} + tl_{ep}$$

$$286 \quad f_{LS} = 1 - \frac{LTT - TT_{veg} - tl_{epO3}}{tl_{seO3}}; \quad \text{for } TT_{veg} + tl_{ep} < LTT < TT_{leaf}$$

287  $f_{Ls} = 0;$  *for*  $LTT \geq TT_{leaf}$  [16]

288 **1.2.2 Stomatal conductance ( $g_{sto}$ )**

289 The coupled photosynthesis-stomatal conductance ( $A_{net}g_{sto}$ ) model based on Leuning (1995) and  
 290 modified for vapour pressure deficit ( $VPD$ ) is used to estimate  $g_{CO_2}$ , stomatal conductance to  $CO_2$  in  
 291  $\mu\text{mol } CO_2 \text{ m}^{-2} \text{ s}^{-1}$  as described in eq. [17].

292  $g_{CO_2} = [f_{min} + m \times A_{net} \times f_{VPD} / (c_s - \Gamma)]$  [17]

293 where  $f_{min}$  ( $\mu\text{mol m}^{-2} \text{ s}^{-1}$ ) is the minimum daytime  $g_{CO_2}$  (Leuning, 1990). The parameter  $m$   
 294 (dimensionless) is the composite sensitivity of  $g_{CO_2}$  to assimilation rate and vapour pressure deficit  
 295 ( $VPD$ ) with the relationship between  $VPD$  and relative stomatal conductance ( $f_{VPD}$ ) estimated by  
 296 eq. [18].

297  $f_{VPD} = \left(1 + \left(\frac{VPD}{VPD_0}\right)^8\right)^{-1}$  [18]

298 where  $VPD_0$  is an empirical parameter, defined using boundary line analysis, describing the variation  
 299 in relative stomatal conductance with  $VPD$  (Danielsson et al., 2003; Pleijel et al., 2007).  $c_s$  ( $\text{mmol}$   
 300  $\text{mol}^{-1}$ ) is the external  $CO_2$  concentration at the leaf surface and is calculated from the external  $CO_2$   
 301 concentration at the upper surface of the leaf boundary layer  $c_a$  ( $\text{mmol mol}^{-1}$ ) so that

302  $c_s = c_a - \left(\frac{A_{net}}{g_{bCO_2}}\right)$  after Masutomi (2023) where  $g_{bCO_2}$  is the boundary layer conductance to  $CO_2$  (in  
 303  $\text{mol m}^{-2} \text{ s}^{-1}$ ), conversion factors for gases and heat across the boundary layer are given in S1a.

304 Finally,  $g_{CO_2}$  is converted to  $g_{O_3}$  in  $\text{mmol } O_3 \text{ m}^{-2} \text{ s}^{-1}$  by dividing by 1000 and using the conversion  
 305 factor 0.96 which assumes that the ratio of the diffusivities of gases in air are equal to the inverse of  
 306 the square root of the ratio of molecular weights (as described in Campbell & Norman (1998)), see  
 307 also supplementary S1b).

308 **1.2.3 Stomatal ozone flux ( $f_{st}$ )**

309 Stomatal  $[O_3]$  flux ( $f_{st}$  in  $\text{nmol m}^{-2} \text{ s}^{-1}$ ) is calculated after the method described in the UNECE  
 310 Mapping Manual (LRTAP, 2017) described in eq. [19].

311  $f_{st} = C_l \times g_{O_3m/s} \times \frac{r_c}{r_{b,O_3} + r_c}$  [19]

312 Where  $C_l$  is the  $[O_3]$  at the upper surface of the laminar layer of a leaf ( $\text{nmol } O_3 \text{ m}^{-3}$ ). Ozone  
 313 concentration in ppb can be converted to  $\text{nmol m}^{-3}$  by multiplying  $O_3$  in ppb by  $P/(R \times T_{air,k})$  where  
 314  $P$  is the atmospheric pressure ( $1.013 \times 10^5$  in Pascal),  $R$  is the universal gas constant ( $8.31447$   
 315  $\text{J/mol/K}$ ) and  $T_{air,k}$  is surface air temperature in degrees Kelvin. To convert  $g_{O_3}$  ( $\text{mol } O_3 \text{ m}^{-2} \text{ s}^{-1}$ ) to  
 316  $g_{O_3m/s}$  ( $\text{m/s}$ ) we assume a standard temperature ( $20^\circ\text{C}$ ) and  $P$ , divide by 41 to give the conductance  
 317 value in  $\text{m/s}$ . The  $r_c/(r_{b,O_3} + r_c)$  term represents the  $O_3$  deposition rate to the leaf through resistances  
 318  $r_b$  (the quasi-laminar resistance ( $\text{s/m}$ )) and  $r_c$  (the leaf surface resistance ( $\text{s/m}$ )) which allow for both  
 319 stomatal and non-stomatal deposition to the leaf surface.  $r_c$  is  $1/(g_{O_3m/s} + g_{ext})$  where  $g_{ext}$  is  
 320  $1/2500$  ( $\text{s/m}$ ).  $r_{b,O_3}$  is estimated by eq. [20].

321  $r_{b,O_3} = 1.3 \times 150 \times \sqrt{\frac{L}{u_l}}$  [20]

322 Where the factor 1.3 accounts of the differences in diffusivity between heat and  $O_3$  (see S1a),  $L$  is  
 323 the cross wind leaf dimension ( $\text{m}$ ) and  $u_l$  is the windspeed ( $\text{m/s}$ ) at the top of the leaf laminar

324 boundary layer. The leaf boundary layer resistance to CO<sub>2</sub> is estimated using a value of 1.24 for the  
 325 difference between heat and CO<sub>2</sub> in place of the 1.3 value for O<sub>3</sub> (Campbell and Norman, 1998).

### 326 1.3 DO<sub>3</sub>SE-Crop canopy

327 The DO<sub>3</sub>SE crop model uses a multi-layer approach to scale from leaf to the canopy. We assume that  
 328 wind, irradiance, [O<sub>3</sub>] concentration and leaf nitrogen content are the key environmental conditions  
 329 which change with cumulative canopy leaf area index (*LAI*) and influence leaf physiology and  
 330 therefore canopy layer estimates of  $A_{net}$ ,  $g_{O_3}$  and  $g_{ext}$ ; other environmental variables (e.g.,  $T_{air}$  and  
 331  $VPD$ ) are assumed to remain constant over the canopy.

#### 332 1.3.1 Canopy irradiance

333 Changes in irradiance through the canopy are described as sunlit and shaded canopy fractions and  
 334 the associated quantity of direct and diffuse photosynthetically active radiation *PAR* (W/m<sup>2</sup>), these  
 335 are estimated according to increasing levels of cumulative *LAI* using the methods of (Pury and  
 336 Farquhar, 1997); full details are given in the section S2. Application of this method requires the  
 337 canopy to be divided into layers of equal *LAI* (including both green (*LAI<sub>G</sub>*) and brown (*LAI<sub>B</sub>*) *LAI*).

338 *PAR* absorbed per unit leaf area is divided into  $PAR_{dir}$ ,  $PAR_{diff}$  which also includes scattered (re-  
 339 flected by the canopy) beam calculated by,

$$340 \quad PAR_{dir}(LAI) = (1 - \rho_{cb}(\beta)) k_b' I_b(0) \exp(-k_b' LAI) \quad [21]$$

$$341 \quad PAR_{diff}(LAI) = (1 - \rho_{cd}) k_d' I_d(0) \exp(-k_d' LAI) \quad [22]$$

342 Where;  $PAR_{dir}$  is the absorbed beam plus scattered beam *PAR* (Photosynthetically Active Radiation)  
 343 per unit leaf area,  $PAR_{diff}$  is the absorbed diffuse plus scattered diffuse *PAR* per unit leaf area,  $\rho_{cb}$  is  
 344 canopy reflection coefficient for beam *PAR*;  $\rho_{cd}$  is canopy reflection coefficient for diffuse *PAR*;  $k_b'$  is  
 345 beam and scattered beam *PAR* extinction coefficient;  $k_d'$  is diffuse and scattered diffuse *PAR*  
 346 extinction coefficient;  $\beta$  is the solar elevation above the horizontal plane of the Earth's surface;  $I_b(0)$   
 347 beam *PAR* per unit ground area at the top of the canopy;  $I_d(0)$  is diffuse *PAR* per unit ground area at  
 348 the top of the canopy.

349 Estimates of the *LAI* fractions of sunlit ( $LAI_{sun}$ ) and shaded ( $LAI_{sh}$ ) parts of each canopy layer (*i*)  
 350 are made by eq. 23 and 24.

$$351 \quad LAI_{sun,i} = \left[ 1 - \exp\left(-0.5 \times \frac{LAI_i}{\sin\beta}\right) \right] \times 2\sin\beta \quad [23]$$

352 Where  $\beta$  is the solar elevation angle (see section S3)

$$353 \quad LAI_{sh,i} = LAI_i - LAI_{sun,i} \quad [24]$$

354 The DO<sub>3</sub>SE-Crop model simulates *LAI* as part of the crop growth model and *LAI* is assumed to be  
 355 evenly distributed across all layers (see section 1.4.2 and eq. 43).

356 Therefore, *PAR* for the sunlit part of each layer ( $PAR_{sun}$ ) can be described as

$$357 \quad \int_{LAI_i}^{LAI_n} PAR_{sun} = \int_{LAI_i}^{LAI_n} (LAI_{sun,i}) \times (PAR_{sh} + PAR_{bsun}(\beta)) dLAI$$

358 Where;  $PAR_{sh}$  is absorbed *PAR* by shaded leaves per unit leaf area and  $PAR_{bsun}$  beam *PAR*  
 359 absorbed by sunlit leaves per unit leaf area; and where  $\int_{LAI_i}^{LAI_n} PAR_{dir}$  can be written as  $(1 - \rho_{cb}$   
 360  $(\beta)) \times k_b' \times I_b(0) \times [exp(-k_b' LAI_i) - exp(-k_b' LAI_n)]$  and  $PAR_{bsun}(\beta) = (1 - \sigma) I_b(0) \frac{\cos\alpha_i}{\sin\beta}$

361 Where;  $\alpha_l$  is angle of irradiance beam on the leaf normal;  $\sigma$  is leaf scattering coefficient for PAR

362 Similarly, PAR for the shaded part of each layer ( $PAR_{sun}$ ) can be described as

$$363 \int_{LAI_i}^{LAI_n} PAR_{sh} = \int_{LAI_i}^{LAI_n} (LAI_{sh,i}) \times (PAR_{diff} + PAR_{bsun}) dLAI$$

364 Where  $\int_{LAI_i}^{LAI_n} (PAR_{diff} (LAI))$  can be written as  $(1 - \rho_{cd}) \times k_b' \times Ib(0) \times [exp(-k_d' LAI_i) -$   
 365  $exp(-k_d' LAI_n)] dL$  and  $\int_{LAI_i}^{LAI_n} PAR_{bs} (LAI)$  is  $I_b(0) [PAR_{dir} - (1 - \sigma)k_b \times [exp(-k_b LAI_i) -$   
 366  $exp(-k_b LAI_n)]$  and  $PAR_{bs} (LAI)$  is absorbed scattered beam PAR per unit leaf area.

### 367 1.3.2 Canopy [O<sub>3</sub>] concentration

368 O<sub>3</sub> concentration will vary as a function of O<sub>3</sub> loss to the canopy (i.e. deposition via the stomates and  
 369 external plant parts) and O<sub>3</sub> replacement from ambient air concentrations above the canopy. Limited  
 370 data have been collected showing how O<sub>3</sub> concentrations vary with canopy depth in semi-natural  
 371 communities (Jaggi et al., 2006). These data suggest that a minimum, bottom canopy O<sub>3</sub>  
 372 concentration ( $C_{zb}$ ), is about 0.2 times that at the top of the canopy ( $C_{zh}$ ) and that the O<sub>3</sub>  
 373 concentration difference within the canopy is closely related to the LAI of the canopy layers.

374 Since each canopy layer can be assumed to be a parallel sink, the O<sub>3</sub> flux to a layer depends on the  
 375 conductance (inverse of resistance) of that layer and the O<sub>3</sub> concentration at the top of the layer ( $C_i$ ;  
 376 with  $C_0$  being  $C_{zh}$  (i.e. the O<sub>3</sub> concentration at height  $C_h$ , the top of the canopy)); we follow and  
 377 generalise the work of Waggoner (1971) by separating the canopy into  $nL$  leaf layers. We calculate  
 378 the O<sub>3</sub> concentration for each layer,  $C_i$ , from O<sub>3</sub> intake,  $I_i$ , by;

$$379 C_i = r_{c,i} I_i \quad [25]$$

380 With  $r_{c,i}$  the leaf surface resistance to O<sub>3</sub> for layer  $i$ .  $I_i$  is calculated as the solution to a system of  
 381 linear equations. Relating  $r_{c,i}$ ,  $I_i$ , and resistances of the bulk air among the leaves ( $R_i$ ), the in-canopy  
 382 aerodynamic resistance for layer  $i$ . Assuming above the canopy there is a uniform O<sub>3</sub> concentration  
 383  $C_0$ , we use generalised equations from Waggoner (1971) for the difference in O<sub>3</sub> concentration  
 384 between the exterior air and leaf interior, which for the top layer is  $C_0$  minus 0, so  $C_0$  and for each  
 385 lower layer the difference is 0. This O<sub>3</sub> concentration difference is calculated by;

$$386 C_0 = R_i \sum_{j=1}^{nL} I_j + r_{c,1} I_1 \quad [26]$$

387 For the top canopy layer,

$$388 0 = R_i \sum_{j=i}^{nL} I_j + r_{c,i} I_i - r_{c,i-1} I_{i-1} \quad [27]$$

389 For each canopy layer  $i$  between the top layer and the bottom layer, and;

$$390 0 = R_{nL+1} I_{nL+1} - r_{c,nL} I_{nL} \quad [28]$$

391 For the bottom layer of the canopy, between the lowest leaf layer and the ground. These can also be  
 392 written into the matrix form;

$$393 \begin{pmatrix} r_{c,1} + R_1 & R_1 & R_1 & \cdots & R_1 \\ -r_{c,1} & r_{c,2} + R_2 & R_2 & \cdots & R_2 \\ 0 & -r_{c,2} & r_{c,3} + R_3 & \cdots & R_3 \\ \vdots & \vdots & \vdots & \ddots & \vdots \\ 0 & 0 & 0 & \cdots & R_{nL+1} \end{pmatrix} \begin{pmatrix} I_1 \\ I_2 \\ I_3 \\ \vdots \\ I_{nL+1} \end{pmatrix} = \begin{pmatrix} C_0 \\ 0 \\ 0 \\ \vdots \\ 0 \end{pmatrix} \quad [29]$$

394 Which can be numerically solved for  $I_x$  when  $r_{c,1} \neq 0$  and  $R_1 \neq 0$ .

395 Resistances for each layer are calculated as described in the supplementary material (section S5)  
396 using standard DO<sub>3</sub>SE deposition modelling methods (Emberson et al., 2012).

### 397 **1.3.3 Canopy maximum carboxylation capacity ( $V_{cmax}$ )**

398 We allow for an exponential decrease in leaf N with canopy depth which will influence both the  
399 photosynthetic capacity ( $V_{cmax}$ ) and hence dark respiration ( $R_{dc}$ ). Photosynthetic capacity at each  
400 canopy layer  $i$  is calculated by eq. [30].

401

$$402 \quad V_{cmax,i} = n_e \times n_0 \times e^{-kN \left(\frac{LAI_i}{LAI}\right)} \quad [30]$$

403 Where  $n_e$  (mol CO<sub>2</sub> m<sup>-2</sup> s<sup>-1</sup> kg C (kg N)<sup>-1</sup>) is a constant relating leaf nitrogen to Rubisco carboxylation  
404 capacity,  $n_0$  (kg N [kg C]<sup>-1</sup>) is the leaf N concentration at the top of the canopy and  $kN$  is a nitrogen  
405 profile co-efficient initially set at 0.78 after (Clark et al., 2011). [In the model, simulations were](#)  
406 [conducted underThe model assumes -non-limiting conditions for soil nitrogen, in accordance with](#)  
407 [the experimental data.](#)

### 408 **1.3.4 Canopy Photosynthesis ( $Anet_c$ )**

409 Net canopy photosynthesis ( $Anet_c$ ) determines the amount of C assimilated by the entire canopy  
410 that can subsequently be allocated to different plant parts (i.e. less than the C respired for plant  
411 growth and maintenance, see section 1.4.1), the amount of C assimilation will ultimately determine  
412 whole plant biomass. The net photosynthesis for each canopy layer ( $Anet_i$ ) is calculated according to  
413 the LAI fraction of that layer that is sunlit ( $LAI_{sun,i}$ ) and shaded ( $LAI_{sh,i}$ ) within the layer ( $i$ ),  
414 multiplied by the net photosynthesis of the sunlit ( $Anet_{sun,i,j}$ ) and shaded leaf ( $Anet_{sh,i,j}$ ),  
415 respectively described by eq. [31] and [32].

$$416 \quad Anet_i = LAI_{sun,i} \times Anet_{sun,i} + LAI_{sh,i} \times Anet_{sh,i} \quad [31]$$

417

418 with  $Anet_c$  calculated by,

$$419 \quad Anet_c = \sum_{i=1}^n Anet_i \quad [32]$$

420  $Anet_c$  is converted from  $\mu\text{mol CO}_2 \text{ m}^{-2} \text{ s}^{-1}$  to  $\text{kg C m}^{-2} \text{ day}^{-1}$  by multiplying by 3600 (converting from  
421 seconds to hours), multiplying by 1.2 (representing the kg of C per mol) and summing each hourly  
422  $Anet_c$  over the course of a day. This  $Anet_c$  is used in the equation 37.

### 423 **1.3.5 Canopy Stomatal Conductance ( $g_{O3_c}$ )**

424 Similarly, canopy layer ( $i$ ) stomatal conductance to O<sub>3</sub> ( $g_{O3_i}$ ), which is converted from  $g_{CO_2}$  by  
425 assuming a diffusivity ratio of 0.96 to convert from CO<sub>2</sub> to O<sub>3</sub> and is calculated by eq. [33] with whole  
426 canopy stomatal conductance calculated by eq. [34].

$$427 \quad g_{O3_i} = LAI_{sun,i} \times g_{O3_{sun,i}} + LAI_{sh,i} \times g_{O3_{sh,i}} \quad [33]$$

$$428 \quad g_{O3_c} = \sum_{i=1}^n g_{O3_i} \quad [34]$$

429 This is converted from  $g_{O3_i}$  in eq. [33] by dividing the conductance value in  $\text{mmol m}^{-1} \text{ s}^{-1}$  by 41000  
430 (assuming standard temperature (20°C) and air pressure ( $1.013 \times 10^5 \text{ Pa}$ )) to give conductance in  
431 m/s.

## 432 **1.4 Crop biomass, LAI, height and yield variables**

433 The following section describes how to estimate crop biomass, important canopy characteristics  
 434 ( $LAI$  and crop height ( $h$ )) and yield variables from accumulated calculations of  $Anet_c$  over the  
 435 course of the growing season following (Osborne et al., 2015).

#### 436 437 **1.4.1 Crop biomass ( $NPP$ and $GPP$ )**

438 The simulation of crop growth requires an estimate of the net primary productivity ( $NPP$ ) which is  
 439 calculated at the end of each day and summed over the growing season. Carbon is assumed to be  
 440 allocated to five key crop components: root, leaf, stem, harvest, and reserve pools (Osborne et al.,  
 441 2015). This carbon allocation is ultimately used to simulate leaf area index ( $LAI$ ), canopy height ( $h$ ),  
 442 biomass, harvest index, and yield at the end of each day throughout the growing season.

443 Net primary productivity  $NPP$  ( $\text{kg C m}^{-2} \text{ day}^{-1}$ ) is accumulated throughout the day using the JULES-  
 444 crop approach to model crop growth (Osborne et al., 2015) described in eq. [35].

$$445 \quad NPP = GPP - R_p \quad [35]$$

446 where  $GPP$  is the gross primary productivity ( $\text{kg C m}^{-2} \text{ day}^{-1}$ ) and  $R_p$  is plant respiration divided into  
 447 maintenance ( $R_{pm}$ ) and growth ( $R_{pg}$ ) respiration ( $\text{kg C m}^{-2} \text{ day}^{-1}$ ) (Clark et al., 2011) where  $R_p =$   
 448  $R_{pm} + R_{pg}$  and where  $R_{pg}$  is assumed to be a fixed fraction of the  $NPP$  as shown in eq. [36].

$$449 \quad R_{pg} = R_{gcoeff} (GPP - R_{pm}) \quad [36]$$

450 Where  $R_{gcoeff}$  is the growth respiration co-efficient which was initially set to 0.25 based on the  
 451 value for all PFTs (i.e. forests and grasses including crops) in (Clark et al., 2011).  $GPP$  is calculated by  
 452 eq. [37].

$$453 \quad GPP = Anet_c + f_{PAW}R_{dc} \quad [37]$$

454 where  $Anet_c$  is net canopy photosynthesis (see eq. 28) and  $f_{PAW}R_{dc}$  is the soil-moisture modified  
 455 canopy dark respiration ( $\text{kg C m}^{-2} \text{ day}^{-1}$ ) where  $R_{dc} = V_{cmax,i} \times R_{dcoeff}$  with  $R_{dcoeff}$  initially  
 456 assumed to be 0.015 based on (Clark et al., 2011);  $V_{cmax,i}$  is the maximum carboxylation efficiency  
 457 for each canopy layer  $i$  which decreases from the top to bottom of the canopy (see eq. 30 ) and  
 458  $f_{PAW}$  is calculated in eq. [7].

459 Leaf maintenance respiration ( $R_{pm}$ ) is assumed equivalent to the soil moisture modified canopy dark  
 460 respiration, while root and stem respiration are assumed to be independent of soil moisture but to  
 461 have the same dependencies on C content. We assume a fixed relationship between C and N  
 462 contents of these organs so that  $R_{pm}$  can be estimated by eq. [38].

$$463 \quad R_{pm} = R_{dc} \times (f_{sw} + (\frac{C_{root} + C_{stem}}{C_{leaf}})) \quad [38]$$

464 The C accumulating as  $NPP$  each day is divided into five carbon pools i.e. root ( $C_{root}$ ), leaf ( $C_{leaf}$ ),  
 465 stem ( $C_{stem}$ ), reserve ( $C_{resv}$ ), and harvest ( $C_{harv}$ ) ( $\text{kg C m}^{-2} \text{ day}^{-1}$ ) according to partition coefficients  
 466 (see eq. [39]) allowing for accumulation of C in these pools over the course of the crop growth  
 467 period.

$$468 \quad \frac{dC_{root}}{dt} = p_{root}NPP,$$

$$469 \quad \frac{dC_{leaf}}{dt} = p_{leaf}NPP,$$

$$470 \quad \frac{dC_{stem}}{dt} = p_{stem}NPP (1 - \tau), \quad [39]$$

$$471 \quad \frac{dC_{harv}}{dt} = p_{harv}NPP,$$

$$472 \quad \frac{dC_{resv}}{dt} = p_{stem}NPP, \tau$$

473 where  $\tau$  is the fraction of stem C that is partitioned into the reserve pool.  $p_{root}$ ,  $p_{leaf}$ ,  $p_{stem}$ ,  
 474  $p_{harv} = 1$ . The partition coefficients are related to the crop development stage ( $DVI$ ) and hence  
 475 effective thermal time ( $TT_{eff}$ ) since emergence. The partition coefficients are based on Osborne et  
 476 al. (2015) and provided as a function of  $DVI$  using six parameters to continuously describe varying  
 477 partition coefficients over the duration of the crop growing season. We use the same multinomial  
 478 logistic as that described in (Osborne et al., 2015) to define this function according to eq. [40].

$$479 \quad p_{root} = \frac{e^{\alpha_{root} + (\beta_{root} DVI)}}{e^{\alpha_{root} + (\beta_{root} DVI)} + e^{\alpha_{stem} + (\beta_{stem} DVI)} + e^{\alpha_{leaf} + (\beta_{leaf} DVI)} + 1},$$

$$480 \quad p_{stem} = \frac{e^{\alpha_{stem} + (\beta_{stem} DVI)}}{e^{\alpha_{root} + (\beta_{root} DVI)} + e^{\alpha_{stem} + (\beta_{stem} DVI)} + e^{\alpha_{leaf} + (\beta_{leaf} DVI)} + 1},$$

$$481 \quad p_{leaf} = \frac{e^{\alpha_{leaf} + (\beta_{leaf} DVI)}}{e^{\alpha_{root} + (\beta_{root} DVI)} + e^{\alpha_{stem} + (\beta_{stem} DVI)} + e^{\alpha_{leaf} + (\beta_{leaf} DVI)} + 1}, \quad [40]$$

$$482 \quad p_{harv} = \frac{1}{e^{\alpha_{root} + (\beta_{root} DVI)} + e^{\alpha_{stem} + (\beta_{stem} DVI)} + e^{\alpha_{leaf} + (\beta_{leaf} DVI)} + 1},$$

483 Where  $DVI$  is the development index;  $\alpha$  and  $\beta$  partition parameters. These parameters describe the  
 484 shape of the thermal time varying partition coefficient for leaves, roots and stems.

485 Once C is no longer partitioned to stems, C from the stem reserve pool will mobilise to the harvest  
 486 pool at a rate of 10% per day following (Osborne et al., 2015) described by eq. [41].

$$487 \quad C_{harv} = C_{harv} + (0.1 C_{resv}) C_{resv} = 0.9 C_{resv} \quad \text{for } p_{stem} < 0.01 \quad [41]$$

488 Total leaf C is divided between green leaf C ( $C_{leaf,green}$ ), and brown leaf carbon ( $C_{leaf,brown}$ ). Carbon  
 489 from the  $C_{leaf,green}$  will mobilise to the harvest pool at the rate of 5% per day after (Osborne et al.,  
 490 2015) and to the  $C_{leaf,brown}$  at a rate of 24% per day once  $f_{LS} > 1$  as described in eq. [42]

$$491 \quad \{C_{harv} = C_{harv} + (0.05 C_{leaf,green}) C_{leaf,green} = 0.86 C_{leaf} \quad C_{leaf} = 0.86 C_{leaf,green} +$$

$$492 \quad 0.24 C_{leaf,brown} \} \quad \text{for } f_{LS} > 1 \quad [42]$$

#### 493 1.4.2 Leaf area Index (LAI) and stem height ( $h$ )

494 At the end of each day, the C content of the stem and leaf is used to estimate  $LAI$  by eqs. [43] and  
 495 [44].

$$496 \quad LAI = (C_{leaf} / f_c) \times SLA \quad [43]$$

$$497 \quad \text{where } SLA = \gamma (DVI + 0.06)^\delta \quad [44]$$

498 The values  $\gamma$  and  $\delta$  were determined by fitting the values to the paired values of  $DVI$  and specific leaf  
 499 area ( $SLA$ ). The value of  $f_c$  is 0.5 (unitless), denotes carbon fraction of dry matter.

500 The amount of C in the stem is used to calculate the crop height  $h$  in m by eq. [45].

$$501 \quad h = k (C_{stem} / f_c)^\lambda \quad [45]$$

502 where  $k$  and  $\lambda$  were determined by fitting the value  $C_{stem}$  and  $h$ .

#### 503 1.4.3 Yield variables

504 According to (Osborne et al., 2015) yield can be calculated from the C allocated to the harvest pool  
 505 ( $C_{harv}$ ) at the end of the growing season as described in eq. [46]

$$506 \quad Yield_{grain} = \frac{(C_{harv} \times (1/f_c) \times D_w \times E_g)}{1000} \quad [46]$$

507 Where harvested C is converted to total biomass (using the conversion factor  $f_c=0.5$ ), i.e., by  
508 multiplying the harvested C by  $1/f_c$ , and then by  $1/0.84 (D_w)$  to account for the grain moisture  
509 content (Mulvaney and Devkota, 2020).  $C_{harv}$  includes both chaff and grain however, O<sub>3</sub> fumigation  
510 experimentalists tend to only include grain when calculating total crop yield at the end of the  
511 growing season, so we assume 15% of the yield is chaff and include a grain to ear ratio,  $E_g$ , of 0.85.  
512 Dividing by 1000 converts yield from kg C m<sup>-2</sup> to g C m<sup>-2</sup>, the unit most often used to describe  
513 experimental yield results.

514 Evaluation of the DO<sub>3</sub>SE-crop model uses a variety of growth 'dry matter (DM)' metrics. Some of the  
515 most important metrics and their calculations are: 'Straw DM' which is calculated as the sum of  
516 carbon allocated to  $C_{stem}$ ,  $C_{leaf}$ , and  $C_{resv}$ ; 'Ear DM' is calculated from  $C_{harv}$  excluding the  
517 moisture content ( $D_w$ ) conversion; 'Grain DM' is calculated from  $C_{harv}$  excluding both the moisture  
518 content ( $D_w$ ) conversion and removing the chaff fraction conversion  $E_g$ ; 'Above ground DM' is the  
519 straw DM plus the Ear DM; 'Below ground DM' is converted from  $C_{root}$ ; and 'Harvest index' is  
520 the Gain DM divided by the Above ground DM. In all cases the  $f_c$  conversion factor is used to  
521 convert from e.g. g C m<sup>-2</sup> to g DM m<sup>-2</sup>.

## 522 2. DO<sub>3</sub>SE-Crop model calibration

### 523 2.1 Xiaoji China experimental dataset

524 The DO<sub>3</sub>SE-crop model was used to analyse the O<sub>3</sub>-FACE (Free Air Concentration Enrichment)  
525 experimental data collected in Xiaoji, Jiangdu, Jiangsu Province, China. The wheat crop was grown in  
526 fully open-air field conditions for three consecutive growing seasons from 2007 to 2009. The dataset  
527 includes four modern cultivars of winter wheat (*Triticum aestivum* L.) grown under ambient (AA) and  
528 elevated (E) O<sub>3</sub>, with the elevated treatment being, on average, 25% above the ambient O<sub>3</sub>  
529 concentrations from early March/April to the end of May each year. The four cultivars were Yannong  
530 19 (strong-gluten wheat, hereafter Y19), Yangmai 16 (medium-gluten wheat, hereafter Y16),  
531 Yangmai 15 (weak-gluten wheat, hereafter Y15), and Yangfumai 2 (weak-gluten wheat, hereafter Y2)  
532 (Zhu et al., 2011).

533 Soil water availability was sufficient for optimum wheat crop growth, so we assumed there was no  
534 soil moisture stress (Feng et al., 2012). Any data gaps were filled following the AgMIP-O3 gap filling  
535 protocol (see S4). For large O<sub>3</sub> data gaps (i.e. greater than 2 weeks) occurring outside the O<sub>3</sub>  
536 fumigation period, we used scaled WFRChem (version 4.2) data for Xiaoji (Conibear et al., 2018) to  
537 ensure consistency in model calibration and potential applications across China. The dataset  
538 provides grain yield components, including the number of ears per square meter, the number of  
539 grains per ear, and the grain dry matter (*Grain DM*, in g/m<sup>2</sup>) (Feng et al., 2011; 2016). Additional  
540 physiological datasets (i.e.  $A_{net}$ ,  $V_{cmax}$ ,  $J_{max}$ , and  $g_{H2O}$  (converted to  $g_{O3}$  as described in S1b)) are  
541 also provided, but only for the year 2008 for all cultivars (Y2, Y19, Y15, and Y16) and for the flag leaf.  
542 The 2008 data also include measurements of the Chlorophyll (in mg m<sup>-2</sup>) which can be used to assess  
543 the level of senescence experienced by the leaf Mariën et al. (2019). Since the year 2008 also  
544 showed significant differences in *Grain DM* between AA and E O<sub>3</sub> treatments (a mean relative yield  
545 difference of 6.73 for all cultivars, see Table S2b) this year was used to train the DO<sub>3</sub>SE-crop model  
546 with other years (i.e., 2007 and 2009) used to test the model.

547 Further experimental details are provided in Feng et al. (2011, 2016). Table 1 describes the average,  
548 minimum and maximum values for all measured variables required to run the DO<sub>3</sub>SE-Crop model  
549 collected at the Xiaoji site for each year. Additionally, the M7 (mean 7-hour O<sub>3</sub> concentration over  
550 the exposure period in ppb) is included for both AA and E O<sub>3</sub> treatments. Measurements were taken  
551 at a height of 2 metres above the ground surface.



552 Table 1. Summary of hourly meteorological and ozone concentration ( $[O_3]$ ) data at Xiaoji.

Variable	Unit	Description	Year 2007 (min, avg, max)	Year 2008 (min, avg, max)	Year 2009 (min, avg, max)
$PAR_{total}$	W/m <sup>2</sup>	Direct and diffuse PAR at the top of the canopy	0, 241.94, 1759	0, 265.15, 1810.48	0, 262.16, 1850.5
$T_{air}$	°C	Surface air temperature in degrees Celsius	-6.35, 10.07, 34.10	-9.22, 8.24, 32.7	-9.17, 9.62, 33.64
$VPD$	kPa	Leaf to air vapour pressure deficit	0, 0.34, 3.77	0, 0.3, 3.5	0, 0.38, 3.8
$u_z$	m/s	Wind speed at a reference height $z$	0.03, 2.14, 8.19	0.07, 2.11, 8.83	0.05, 2.10 8.45
$C_z$ (and M7 value) for AA $O_3$ treatment	ppb	Ozone concentration at a reference height $z$	0, 15.48, 129.95 (47.2)	0, 16.2, 137.07 (49)	0, 15.9, 102.02 (47)
$C_z$ (and M7 value) for E $O_3$ treatment	ppb	Ozone concentration at a reference height $z$	0, 16.83, 176.73 (56.1)	0, 17.46, 171.19 (60.7)	0, 17.95, 153.40 (58.7)
$O_3$ exposure period	Days		38	92	92

553

## 554 2.2 DO<sub>3</sub>SE-Crop calibration and evaluation

555 Development and calibration of the DO<sub>3</sub>SE-Crop model with the Xiaoji experimental data set  
 556 followed three main steps: i). sensitivity analysis to identify key model parameters to calibrate; ii).  
 557 calibration of these key parameters for a single year and both tolerant and sensitive cultivars, and  
 558 iii). evaluation of key DO<sub>3</sub>SE-Crop model outputs for different years and cultivars from those used in  
 559 model calibration.

560 To perform the sensitivity analysis we used the SaLIB python library (Iwanga et al., 2022, Herman  
 561 and Usher, 2017). The analysis requires ranges to be specified for the parameters (identified by an  
 562 initial manual calibration) that are included in the sensitivity analysis. For physiological parameters,  
 563 ranges were determined by considering the range of these parameters in the literature. For carbon  
 564 allocation parameters, the range was identified by considering the maximum and minimum values of  
 565 these parameters that would result in [appropriate dry matter partitioning within the plant](#) realistic  
 566 [plant response](#). Once the ranges were identified, the sensitivity analysis was run using the extended  
 567 fourier amplitude sensitivity analysis, which has been commonly used by other crop modellers to  
 568 improve their calibrations (Silvestro et al., 2017, Vazquez-Cruz et al., 2014) . From the sensitivity  
 569 analysis outputs ([see Fig S6](#)), the parameters whose variation contributes the most to variations in  
 570 selected modelling outputs (in this case photosynthetic rate and yield) were identified as the key  
 571 model outputs for calibration. Using this method we identified the following DO<sub>3</sub>SE-crop parameters  
 572 as those most important to calibrate: (i) leaf photosynthesis parameters ( $V_{cmax25}$ ,  $J_{max25}$ ,  $kN$ ,  $m$ ,  
 573 and  $VPD_0$ ); (ii) C allocation parameters ( $\alpha_{root}$ ,  $\alpha_{leaf}$ ,  $\alpha_{stem}$ ,  $\gamma$ ,  $\tau$ ) and related dark respiration  
 574 coefficients ( $R_{dcoeff}$  and  $R_{gcoeff}$ -) [which](#) were later included in the calibration after identifying  
 575 issues with overestimated respiration, likely due to the use of parameter values designed for broad  
 576 plant functional types, which may not be suitable for wheat).  $O_3$  damage module parameters related  
 577 to senescence ( $\gamma_3$ ,  $\gamma_4$ ,  $\gamma_5$ , and  $CLsO3$ ) were not included in the sensitivity analysis, as  $\gamma_3$  and  $CLsO3$  is

578 already recognized as important for calibration, and  $\gamma_4$  and  $\gamma_5$  were introduced in this study to  
579 represent the start (SOS) and end (EOS) of senescence, making both essential for calibration.  
580 Phenology parameters were also excluded as earlier studies have shown these are relatively  
581 straightforward to calibrate using automated methods for a range of environmental conditions  
582 (Nguyen et al., 2024). We note that assessing the probability distribution of these ranges would also  
583 be useful but consider this outside the scope of the current paper due largely to data limitations.

584 The DO<sub>3</sub>SE-Crop model was then calibrated using the 2008 dataset for the Y2 and Y16 cultivars. The  
585 year 2008 was selected since this showed a substantial difference in yield of 208 and 148 g/m<sup>2</sup>  
586 between the AA and EO<sub>3</sub> treatments for the Y2 and Y16 cultivars respectively. These cultivars were  
587 chosen since they were identified as the most sensitive (Y2) and tolerant (Y16) cultivars according to  
588 the experimental analysis conducted by Feng et al. (2016). [See Fig. 5, which shows a diagram](#)  
589 [representing the calibration process.](#)

590 Calibration of the phenology module used only the Y2 cultivar, AA O<sub>3</sub> treatment data describing the  
591 timing of emergence, anthesis and maturity to calibrate key phenology parameters ( $T_b$ ,  $T_0$ ,  $T_m$ ,  
592  $VT_{min}$ ,  $VT_{max}$ ,  $PIV$ , and  $PID$ ,  $TT_{emr}$ ,  $TT_{veg}$ ,  $TT_{rep}$ , and  $T_l$ ). The phenology calibration was  
593 automated by computationally applying a genetic algorithm (Wang, 1997), an optimisation  
594 technique with gradient decent to find the best parameters. This uses a combination of crossover  
595 strategy (selecting parameters randomly from parameter pairings) and mutation strategy (which  
596 takes a parameter range and uses incremental step changes) to identify the parameters which give  
597 the highest R<sup>2</sup>, and lowest root mean square error (RMSE) when compared with observations of the  
598 timing (day of year) of anthesis and maturity.

599 Calibration of the leaf physiology, canopy C allocation and O<sub>3</sub> damage DO<sub>3</sub>SE-Crop modules was  
600 performed manually. This required that an initial value and range be defined for each parameter.  
601 which were defined from a combination of observations from the Xiaoji experimental dataset as well  
602 as values taken from the literature (see Table A1 and A2 of the Appendix A for details). The model  
603 was manually calibrated until certain conditions were satisfied, as explained below.

604 Calibration of the leaf physiology parameters ( $V_{cmax}$ ,  $J_{max}$ ,  $kN$ ,  $m$ , and  $VPD_0$ ) was performed only  
605 the Y2 cultivar, AA O<sub>3</sub> treatment whilst keeping all other parameters fixed. This calibration aimed to  
606 achieve a maximum  $A_{net}$  value of 30  $\mu\text{mol CO}_2 \text{ m}^{-2} \text{ s}^{-1}$  and a  $g_{O_3}$  value of 350  $\text{mmol O}_3 \text{ m}^{-2} \text{ PLA s}^{-1}$ ,  
607 consistent with the maximum values observed in the Xiaoji dataset (Zhu et al., 2011). We calibrated  
608  $V_{cmax}$  and  $J_{max}$  as measurements are only provided for Y2 and Y16 cultivars and only for certain  
609 points during the growth period and we know that  $V_{cmax}$  and  $J_{max}$  can vary seasonally.

610 Calibration of the C allocation parameters ( $\alpha_{root}$ ,  $\alpha_{leaf}$ ,  $\alpha_{stem}$ ,  $\gamma$ ,  $\tau$  and related dark respiration  
611 coefficients ( $R_{dcoeff}$  and  $R_{gcoeff}$ ), was also performed keeping all other parameters fixed. This  
612 calibration aimed to achieve the following criteria:- a stem dry matter to leaf dry matter ratio ( $R_{SL}$ )  
613 of approximately 2:1 (Huang et al., 2022); relative growth of different plant parts (i.e. leaves, stem,  
614 roots, grain) consistent with profiles found in the literature (Osborne et al., 2015; de Vries et al.,  
615 1989); a modelled *Grain DM* within  $\pm 30\%$  of the observed; an *above ground DM* value of  
616 between 1200-1600  $\text{g m}^{-2}$ ; an *LAI* value between 4-7  $\text{m}^2 \text{ m}^{-2}$ ; and an  $R_d$  value of between 30 to 60%  
617 of  $A_{net}$  (Amthor et al., 2019). We calibrated C allocation parameters as in the JULES-crop model  
618 calibration has only been performed for broad, global scale application for wheat (Osborne et al.,  
619 2016) and therefore requires further calibration for application under Chinese conditions. Further,  
620 the observed dataset does not provide any information with regards to the change in carbon  
621 allocation parameters due to ozone. The C allocation parameters were only calibrated for ambient  
622 ozone conditions, and we only investigate the effect of ozone on C assimilation (not C allocation).

623 Finally, calibration of the O<sub>3</sub> parameters ( $\gamma_3$ ,  $\gamma_4$  and  $\gamma_5$ ) was performed using 2008 data for both the  
624 Y2 and Y16 cultivars whilst again keeping the other parameters fixed. Calibration was targeted so

625 that the difference in *Grain DM* between ambient and elevated O<sub>3</sub> treatments as close as possible  
626 to ± 10% of the observed.

627 The manual calibration process consisted of three stages as explained above, as well as comparisons  
628 with established information on wheat growth from the literature. By reducing the number of  
629 parameters involved in the calibration, the chance of equifinality (multiple combinations of  
630 parameters yielding similar results) was minimised (Beven, 2006). The parameters identified by the  
631 sensitivity analysis were varied within realistic ranges to obtain a parameterization that closely  
632 approximates wheat physiological processes. Multiple parameterizations were tested to avoid  
633 convergence on local minima in R<sup>2</sup> and RMSE. While further fine-tuning of the parameter ranges  
634 could potentially improve yield prediction, it might also disrupt simulations of other key plant  
635 processes, such as carbon allocation or photosynthesis. The calibration approach balances the need  
636 for accurate output simulation with the physiological realism required for wheat growth under the  
637 conditions of this study. Though it is difficult to claim that the absolute optimal parameter set has  
638 been achieved, this limitation is common to any model calibration (Wallach, 2011). The current  
639 parameterisation represents a physiologically realistic simulation of wheat growth under the  
640 conditions of the present study using a robust calibration method.

641 Evaluation of the DO<sub>3</sub>SE-Crop model was conducted using Xiaoji data for 2007 and 2009 for all  
642 cultivars, and 2008 data for Y19 and Y16 cultivars. This evaluation tested the ability of the calibrated  
643 DO<sub>3</sub>SE-Crop model to simulate *Grain DM* using R<sup>2</sup> and RMSE statistical tests.

644

645

## 646 Results

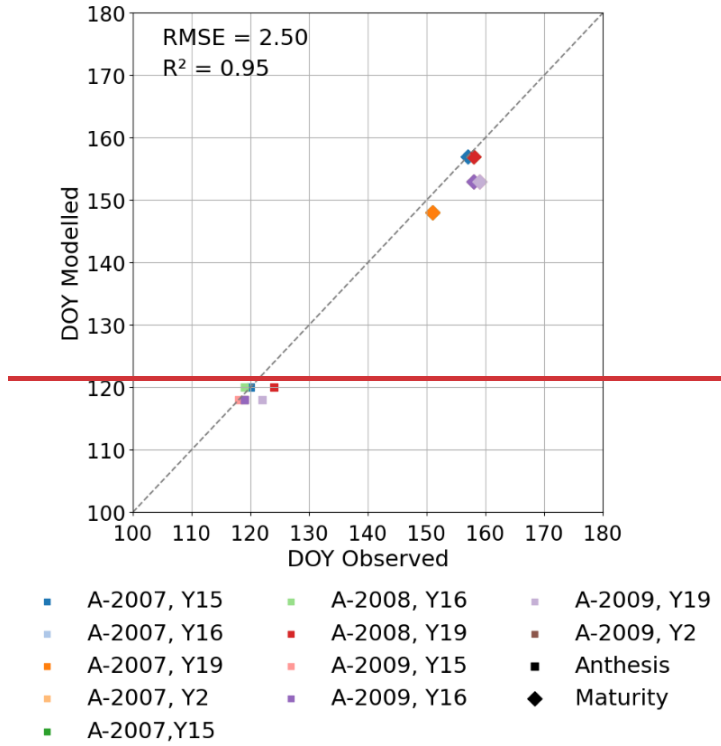
647 We first examine the model's ability to simulate the key phenological development stages since this  
648 is key to simulating the variation in C allocation to different plant parts over the course of the  
649 growing season and hence how O<sub>3</sub> exposure will influence growth and yield which is determined by  
650 the timing and length of the grain filling period. We also explore how DO<sub>3</sub>SE-Crop simulates within  
651 canopy [O<sub>3</sub>] profiles to understand which layers of the canopy are most important in determining O<sub>3</sub>  
652 response. We then examine the ability of the model to simulate leaf-level physiology and C  
653 allocation to the different parts of the crop. Lastly, the impact of both instantaneous and long-term  
654 O<sub>3</sub> damage on the crop's final *Grain DM* is evaluated for different cultivars and years.

### 655 i) Crop Phenology

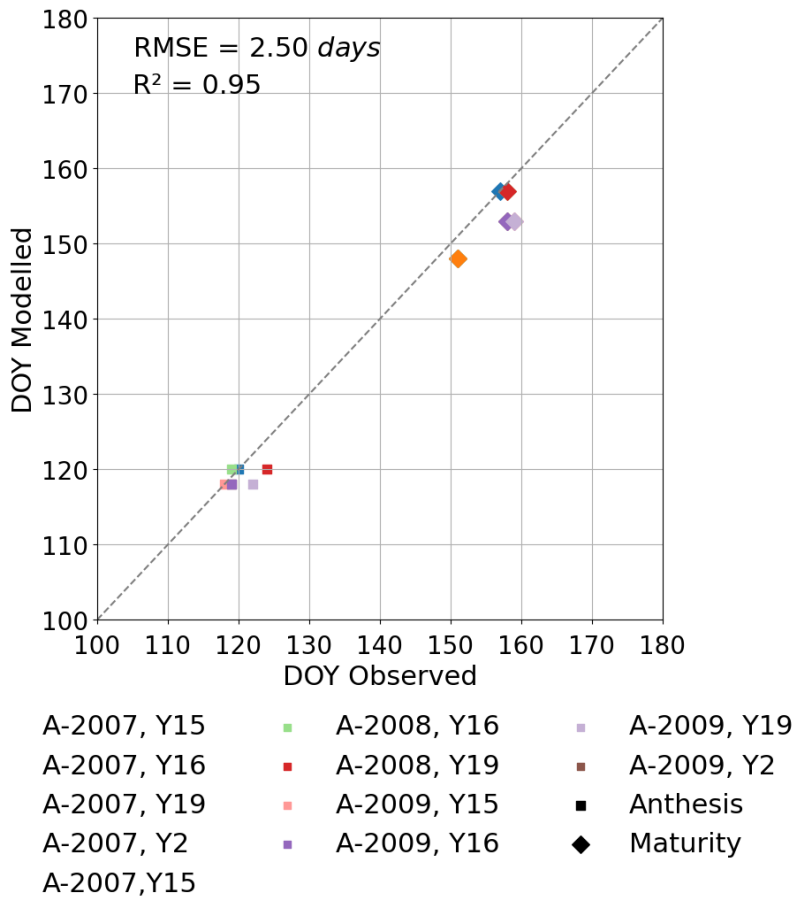
656 The Xiaoji dataset provides sowing and harvest dates for all cultivars for each year but only provides  
657 the date of the timing of anthesis for the years 2008 and 2009 for all cultivars. We assume that DVI =  
658 1 is equivalent to the start of anthesis and that this occurs 4-5 days after flag leaf emergence as  
659 shown in Fig. 2. We determine the influence of O<sub>3</sub> on the start and end of senescence (SOS and EOS)  
660 using the breakpoint method (described in Pande et al., 2024) to assess significant changes in the  
661 chlorophyll values that indicate senescence onset and rate of change for the quantification of  $tl_{ep}$   
662 and  $tl_{se}$ . This method is applied for chlorophyll data collected in 2008 under both AA and E O<sub>3</sub>  
663 treatments for the Y2 cultivar. We then assume that these key phenology parameters (i.e.,  $TT_{emr}$ ,  
664  $TT_{veg}$ ,  $TT_{rep}$ ,  $tl_{ep}$  and  $tl_{se}$ ) are consistent across cultivars and years. Our results in Fig 3 suggests  
665 this is a reasonable assumption however, we appreciate that assuming these phenology parameters  
666 will work for a wider variety of cultivar types (e.g., early or late sown and/or maturing) and years  
667 with rather different meteorological conditions, needs to be done with caution.

668 Fig S1 shows the modelled vs observed timing of anthesis and harvest for the training dataset. Fig 3  
669 shows the same for the test dataset. For the test dataset there is a variation of 2 to 4 days and 1 to 6  
670 days for the modelled anthesis and maturity in relation to observed anthesis and maturity  
671 respectively, with observed phenology tending to be a little later than modelled. The  $T_l$  ranges  
672 between 1325 and 1478 °C days for the three years, with crop sowing occurring between 315 and  
673 324 days of year and harvests occurring between 135 and 151 day of year (of the following year).  
674 The number of days from the modelled crop sowing to harvest was between 181 and 191 for the  
675 three years, compared to 198 and 201 for the observations.

676 Fig. 3 Modelled vs observed phenological stages provided as day of year (DOY) for the test dataset  
 677 (i.e., excluding the year 2008 for the Y2 cultivar).



678  
679



680

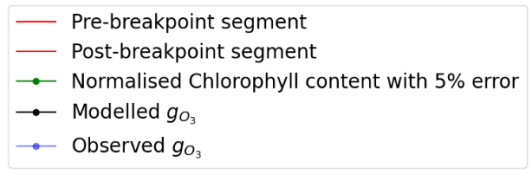
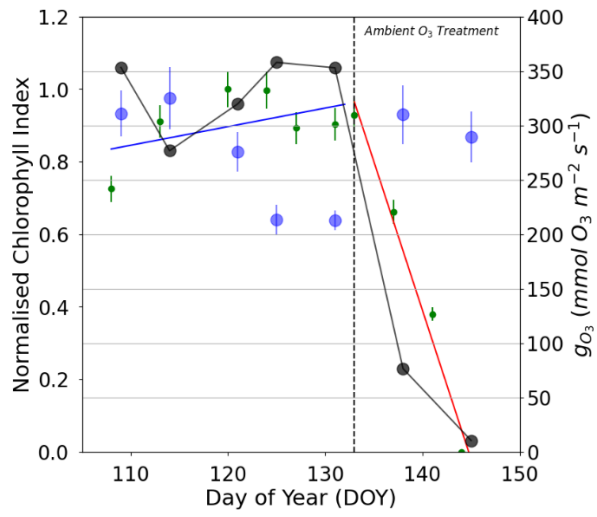
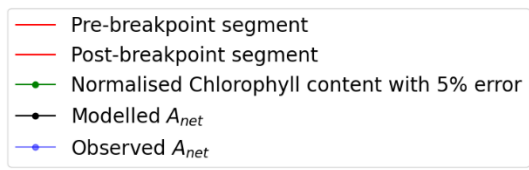
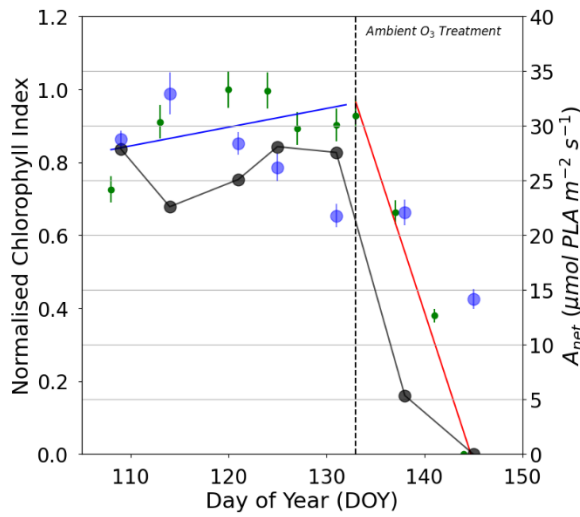
681 ii-a) Leaf physiology variables ( $A_{net}$ ,  $g_{O_3}$ )

682 The DO<sub>3</sub>SE-Crop model was able to simulate the seasonal  $A_{net}$  and  $g_{O_3}$  with values ranging from 0 to  
683 27  $\mu\text{mol CO}_2 \text{ m}^{-2} \text{ s}^{-1}$  and 10 to 351  $\text{mmol O}_3 \text{ m}^{-2} \text{ s}^{-1}$  for  $A_{net}$  and  $g_{O_3}$  respectively over the course of  
684 the growing season (see Fig 4). The simulated daily maximum values of modelled  $g_{O_3}$ , at 351  $\text{mmol}$   
685  $\text{O}_3 \text{ m}^{-2} \text{ s}^{-1}$ , were within the range of the observed value of 340  $\text{mmol O}_3 \text{ m}^{-2} \text{ s}^{-1}$ . Similarly, the  
686 modelled daily maximum  $A_{net}$  is 27  $\mu\text{mol CO}_2 \text{ m}^{-2} \text{ s}^{-1}$  compared to observed value of 28  $\mu\text{mol CO}_2 \text{ m}^{-2}$   
687  $\text{s}^{-1}$  for the period between anthesis and 10 days before maturity for the year 2008, for the Y16  
688 cultivar (similar results were obtained for the Y2 cultivar; see Fig. S5). In Fig. 4a and b, the steep  
689 decline in modelled  $A_{net}$  and  $g_{O_3}$  is not seen in the observed dataset. This discrepancy may occur  
690 since the simulated  $A_{net}$  and  $g_{O_3}$  values represent sunlit parts of the upper canopy which comprise  
691 both green and senesced leaf material. In contrast, observed  $A_{net}$  and  $g_{O_3}$  values are measured  
692 specifically on the flag leaf and most likely only for the green parts of the leaf, since the LI-6400  
693 photosynthesis system mounted with a 6400–40 leaf chamber fluorometer (used to measure  $A_{net}$   
694 and  $g_{O_3}$  in the Xiaoji experiment, Feng et al., 2016) will not provide values for senesced leaf  
695 material. See also Figure 4 which combines  $A_{net}$  and  $g_{O_3}$  with observed normalised chlorophyll  
696 content and clearly shows the leaf is senescing as predicted by the model. However, the decline in  
697 observed chlorophyll values aligns well with the decline in modelled  $A_{net}$  and  $g_{O_3}$  with the timing of  
698 the earlier onset of senescence by 0-3 days between the AA and E O<sub>3</sub> treatments being captured well  
699 by the model. It is useful to note that the calibrated  $V_{cmax}$  and  $J_{max}$  values match the observed  
700 values within  $\pm 2 \mu\text{mol CO}_2/\text{m}^2/\text{s}$ .

701 Fig 4. Comparison of daily maxima seasonal profiles of DO<sub>3</sub>SE-Crop modelled canopy leaf vs observed  
702 flag leaf data for a). AA O<sub>3</sub> treatment  $A_{net}$ , and b). AA O<sub>3</sub> treatment  $g_{O_3}$  and c) E O<sub>3</sub> treatment  $A_{net}$ ,  
703 and d). E O<sub>3</sub> treatment  $g_{O_3}$  for the period from the anthesis (i.e.,  $TT_{rep}$ ) for the year 2008 and the  
704 Y16 cultivar. The left (solid blue line) and right (solid red line) represent the segment fits to the  
705 normalised chlorophyll content values for application of the breakpoint method to define the SOS  
706 (Start of Senescence) shown as the solid black dashed line. The green scatter solid dots, along with  
707 their standard measurement error, represent the normalised observed chlorophyll content values  
708 (see Fig 7 for further details).

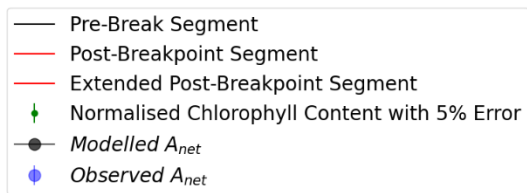
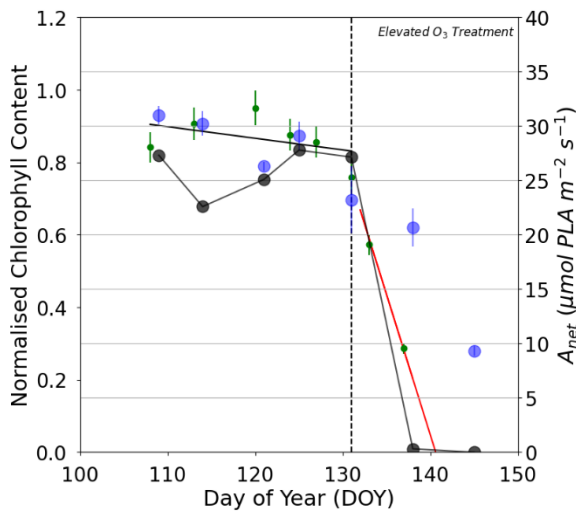
709 a).

b).

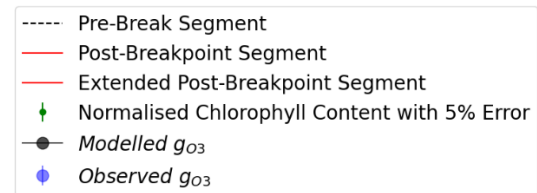
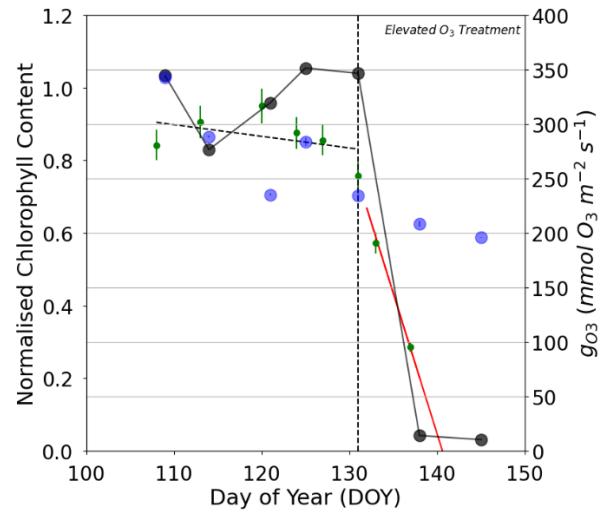


710

711 c).



d).



712

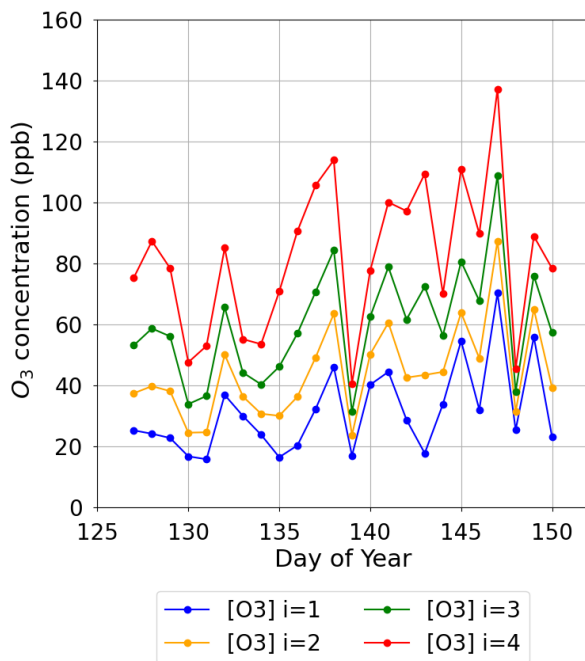
713

714 iii-b). Within canopy variation in  $O_3$  and physiology

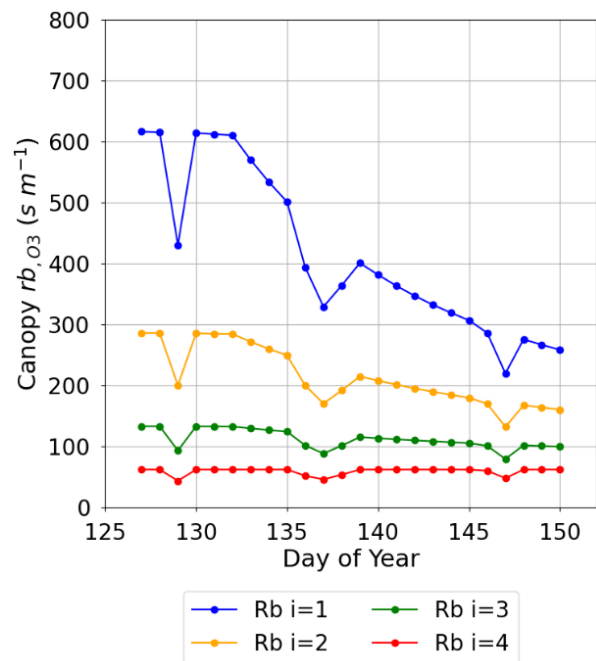
715 An important determinant of  $O_3$  deposition and damage is stomatal  $O_3$  deposition (our  $gO3_c$ ) which  
 716 is a function of within canopy transfer of  $O_3$  and stomatal and non-stomatal deposition. The multi-  
 717 layer aspect of the DO<sub>3</sub>SE-Crop model allows within canopy stomatal and non-stomatal  $O_3$   
 718 deposition to be simulated. Fig 5 shows the variation in key variables that determine total and  
 719 stomatal  $O_3$  canopy deposition across 4 canopy layers as a mid-day average over the course of the  
 720  $tl_{ep}$  period of the flag leaf, for the year 2008 and the Y16 cultivar.

721 Fig 5. Plot showing variation in key  $O_3$  deposition terms as daily maxima by canopy layer (N.B.  $i = 4$   
 722 is the top canopy layer,  $n = 4$ ) a).  $O_3$  concentration at the top of each layer, b). leaf boundary layer  
 723 resistance by canopy layer ( $rb_{,O_3}$ ), c). PAR for the sunlit LAI component of each layer ( $PAR_{sun}$ ) and  
 724 d). leaf level stomatal conductance to  $O_3$  ( $g_{O_3}$ ) for the period from anthesis (i.e.,  $TT_{rep}$ ) for the Y16  
 725 cultivar and for the E  $O_3$  treatment in 2008.

726 a).

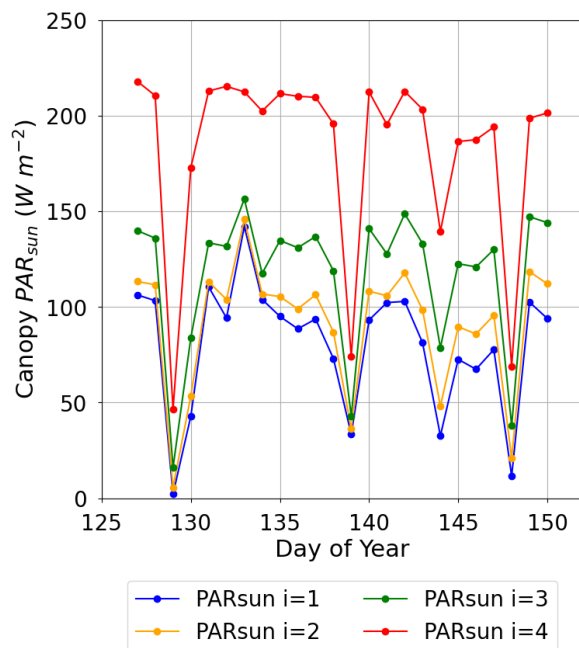


b).

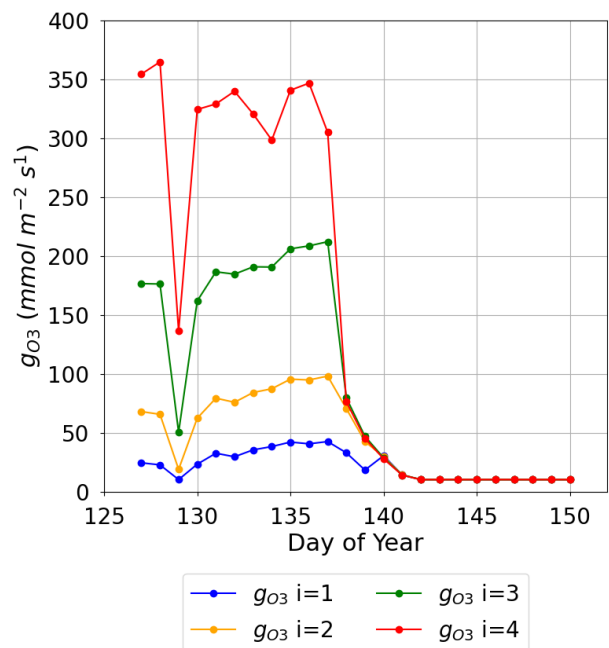




728 c).



d).



729

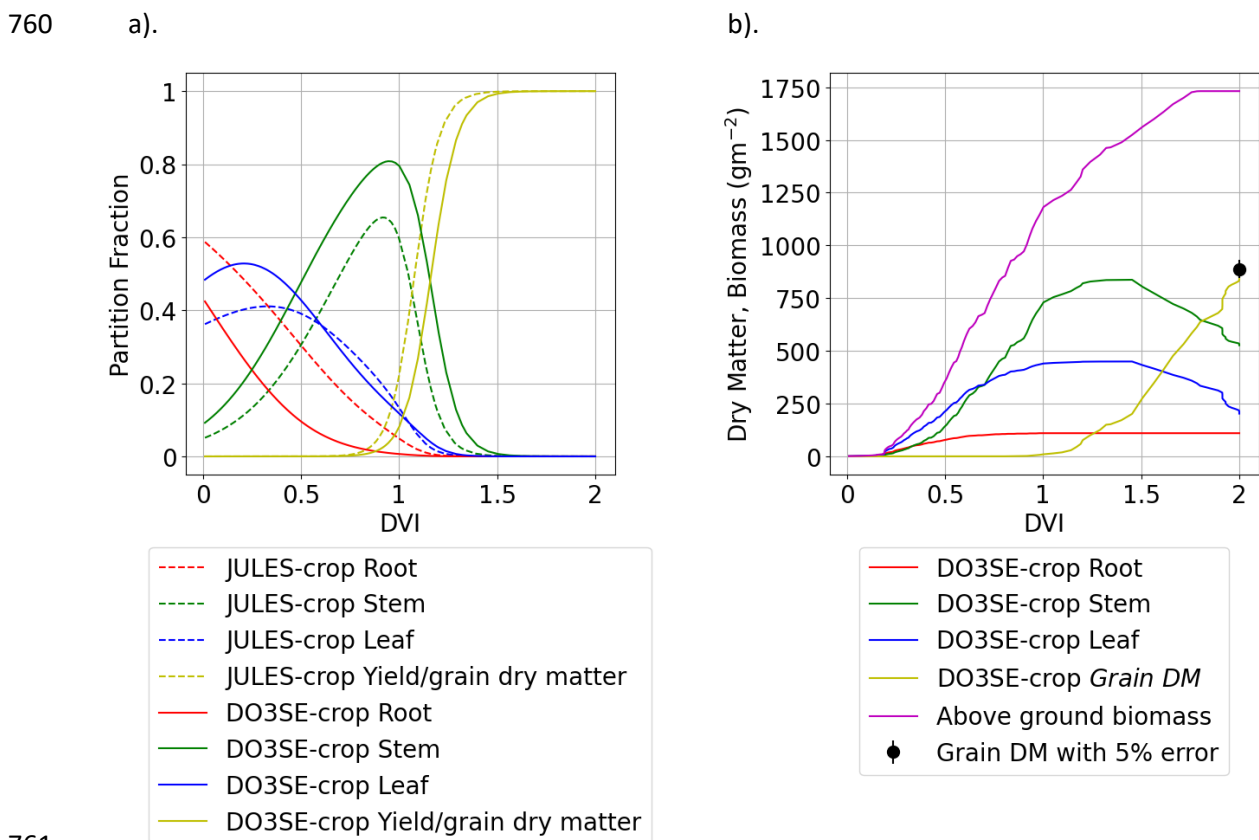
730 Figure 5a. shows a decrease of within canopy  $O_3$  concentration from highs of around 140 ppb to  
 731 values within the range of 10 to 50 ppb between the top of the canopy and bottom canopy layer, the  
 732 penetration of  $O_3$  into the canopy increases over time as the canopy senescence and  $O_3$  uptake is  
 733 reduced. Similarly,  $PAR_{sun}$  reduces from maximum values of around  $200 \text{ W m}^{-2}$  at the top of the  
 734 canopy to values of around  $100 \text{ W m}^{-2}$  in the lower canopy layers even on sunny days (see Fig. 5c).  
 735 The leaf  $rb_{O_3}$  (Fig. 5b) increases with canopy depth with resistances in the region of approximately  
 736  $50 \text{ s m}^{-1}$  at the top of the canopy to values of around  $600 \text{ s m}^{-1}$  at the bottom of the canopy, this will  
 737 limit stomatal  $O_3$  uptake in the lower canopy layers, finally these factors combine to influence  
 738 canopy level  $g_{O_3}$  (Fig. 5d) which reduces from values of around 350 at the top of the canopy to 20  
 739  $\text{nmol } O_3 \text{ m}^{-2} \text{ s}^{-1}$  at the bottom of the canopy layer, these differences in leaf  $rb_{O_3}$  and  $g_{O_3}$  reduce with  
 740 the onset of senescence. This analysis shows the importance of interplay between these different  
 741 factors for an accurate whole canopy estimate of  $O_3$  deposition.

742 **iv)** Crop development, biomass and yield.

743 The dry matter dynamics of the different parts of the crop are shown in Fig. 6. The modelled  
 744  $Grain DM$  value of  $851 \text{ g m}^{-2}$  was reasonably close to the observed value of  $888 \text{ g m}^{-2}$ . The stem to  
 745 leaf dry matter ration ( $R_{SL}$ ) is 2.1:1 and therefore in the range provided in the literature (Huang et  
 746 *al.*, 2022). The above-ground biomass values of  $1510 \text{ g m}^{-2}$  also match reasonably well against the  
 747 1200 to  $1600 \text{ g m}^{-2}$  range described in the literature (Huang et al., 2022; Liu et al., 2022). Further, the  
 748 partition fraction profiles are consistent with those of Osborne *et al.* (2015) as shown in Fig. 6a) with  
 749 the main differences being that the modelled stem and root partition profiles are somewhat higher  
 750 and lower, respectively. The JULES model comparison is provided for illustrative purposes only (i.e.  
 751 this model has not been calibrated with the Xiaoji data but rather is a parameterisation suggested  
 752 for global application).

753 Fig 6. Seasonal profiles (i.e., plotted against  $DVI$ ) of carbon allocation variables for the Xiaoji  
 754 calibrated  $DO_3SE$ -Crop model (i.e. AA  $O_3$  treatment, year 2008 and Y16 cultivar) with a). showing the  
 755 partition fractions of the daily accumulated  $NPP$  partitioned to roots, stems, leaves, and grains for  
 756 the Xiaoji calibrated  $DO_3SE$ -Crop model (solid lines) vs the JULES Crop model (dashed line) calibrated

757 for global application after Osborne *et al.* (2015)) and b). showing the *DM* (in g/m<sup>2</sup>) of daily  
 758 accumulated *NPP* partitioned to roots, stems, leaves, and grains with the observed final *GrainDM*  
 759 for Y16 cultivar in 2008 also shown (solid black dot with 5% error).



Year	Tolerant: Instantaneous O <sub>3</sub> effect on % <i>Grain DM</i>		Tolerant: Long-term O <sub>3</sub> effect on % <i>Grain DM</i>	
	Ambient versus pre-industrial	Elevated versus pre-industrial	Ambient versus pre-industrial	Elevated versus pre-industrial
2007	<del>00</del>	<del>0.20</del> 0.01	<del>16.60</del> 18.43	<del>29.05</del> 31.13
2008	<del>00</del>	<del>00</del>	<del>9.85</del> 13.43	<del>24.37</del> 29.14
2009	<del>0.03</del> 0.03	<del>0.03</del> 0.03	<del>17.48</del> 19.5	<del>25.87</del> 28.11
Year	Sensitive: Instantaneous O <sub>3</sub> effect on % <i>Grain DM</i>		Sensitive: Long-term O <sub>3</sub> effect on % <i>Grain DM</i>	
	Ambient versus pre-industrial	Elevated versus pre-industrial	Ambient versus pre-industrial	Elevated versus pre-industrial
2007	<del>00</del>	<del>0.01</del> 0.2	<del>18.43</del> 16.60	<del>31.13</del> 29.05
2008	<del>00</del>	<del>00</del>	<del>13.43</del> 9.85	<del>29.14</del> 24.37
2009	<del>0.01</del> 0.01	<del>0.01</del> 0.01	<del>19.51</del> 17.48	<del>28.11</del> 25.87

782

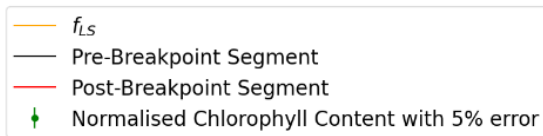
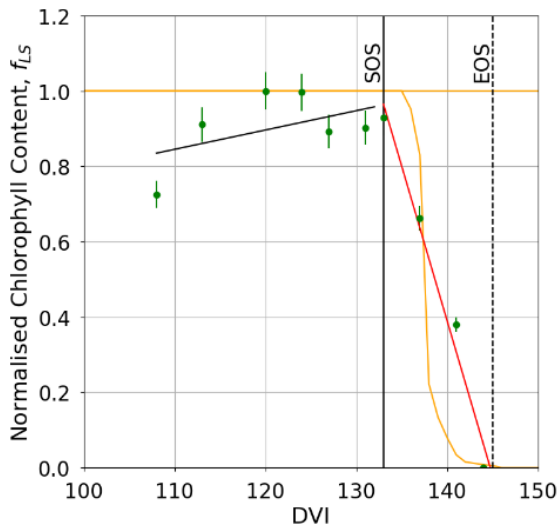
783 [iv.bvi](#) Senescence

784 The breakpoint method (Mariën et al., 2019) was used to determine the onset (SOS) and end (EOS)  
785 of senescence and maturity respectively using the chlorophyll data which was available for the year  
786 2008, and the Y16 and Y2 cultivars. Results in Fig. 7 and Fig. S4 show that the E-O<sub>3</sub> treatment for  
787 cultivars Y16 and Y2 brought forwards the SOS by 3 and 5 days (see Fig. 7) respectively, and EOS by 6  
788 and 9 days (see Fig. S4) respectively. Fig 7 also shows the  $f_{LS}$  profile which denotes the DO<sub>3</sub>SE-Crop  
789 models accumulated stomatal O<sub>3</sub> flux effect on senescence, it is clear that  $f_{LS}$  is able to simulate the  
790 change in normalised chlorophyll content reasonably well. The slope of the ambient  $f_{LS}$  is already  
791 steep since the ambient treatment already has rather high O<sub>3</sub> levels as is now made clear in Table 1  
792 with a value of 47ppb. According to the M7 wheat dose-response relationship this would result in a  
793 yield loss of ~ 5%.

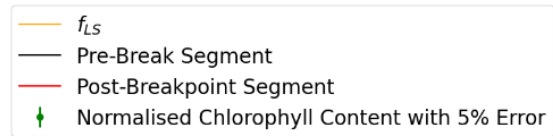
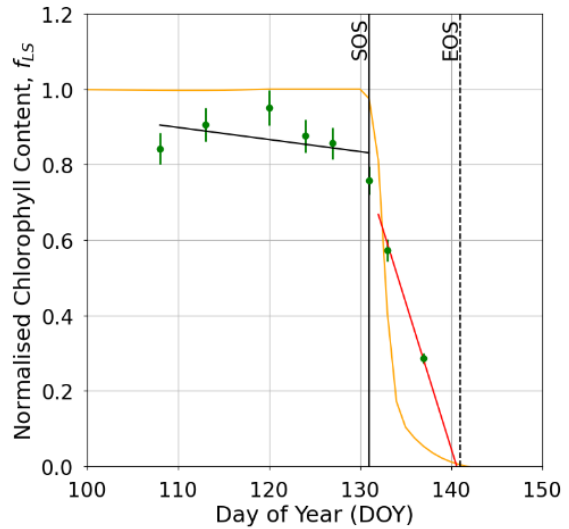
794 Fig 7. Profiles of O<sub>3</sub> induced leaf senescence for the Y16 cultivar for the a). AA O<sub>3</sub> treatment and b). E  
795 O<sub>3</sub> treatment. The timing of the SOS (solid black line) and EOS (dashed black line) were determined  
796 by applying the break point method to the chlorophyll data and are shown in relation to the  $f_{LS}$   
797 simulations of senescence (yellow solid line). The observed normalised chlorophyll content data,  
798 shown as filled blue symbols, include error bars representing the standard deviation of the  
799 measurements.

800

801 a).



801 b).



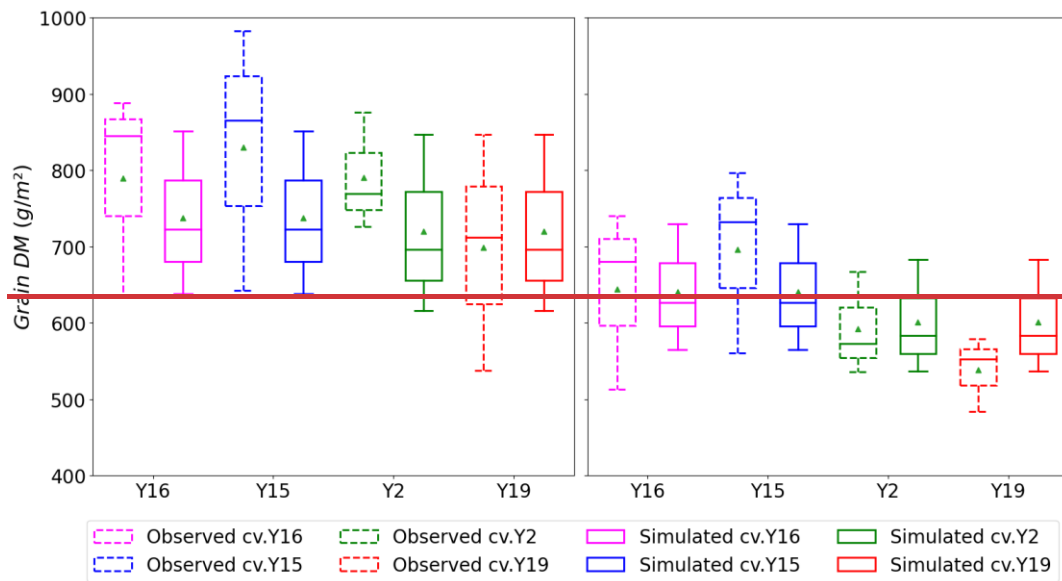
802

803 [viiiiv-e](#). Grain DM simulations across years and between cultivars

804 Fig. 8 shows a box plot of the modelled vs observed *Grain DM* for both the sensitive (Y2, Y19) and  
 805 tolerant (Y15, Y16) cultivars for each O<sub>3</sub> treatment (AA and E) for the years 2007, 2008 and 2009 (i.e.  
 806 all data). Given the variability in the experimental data the model simulates the difference in  
 807 *Grain DM* between the AA and E O<sub>3</sub> treatments reasonably well with a simulated reduction in  
 808 *Grain DM* of 29 to 131 g m<sup>-2</sup> compared with observed values of 81 to 165 g m<sup>-2</sup> for the tolerant; and  
 809 49 to 196 g m<sup>-2</sup> compared with observed values of 54 to 293 g m<sup>-2</sup> for the sensitive cultivars  
 810 respectively. The most notable difference is that there is a larger range in the simulated  
 811 *Grain DM* losses of the modelled sensitive cultivars though the simulated mean value for absolute  
 812 *Grain DM* suggests a more conservative influence of O<sub>3</sub> with yields at 610 g m<sup>-2</sup> vs observed average  
 813 yields of 590 g m<sup>-2</sup>.

814

815 Fig 8. Boxplots (crosses: 0.01 and 0.99 percentiles; box: 0.25 quartile, median and 0.75 quartile;  
 816 triangle: mean) of simulated and observed wheat *Grain DM* for the tolerant (Y15 and Y16) and  
 817 sensitive (Y2 and Y19) cultivars under a.) AA and b.) E O<sub>3</sub> treatment for the years 2007, 2008 and  
 818 2009; these data include all the dataset.

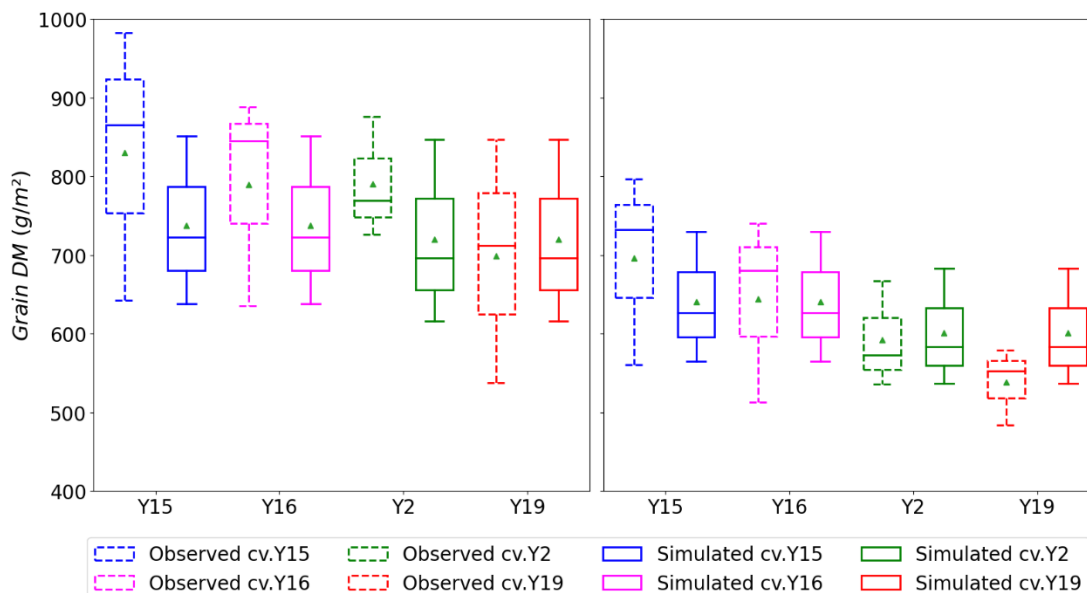


819

820

a).

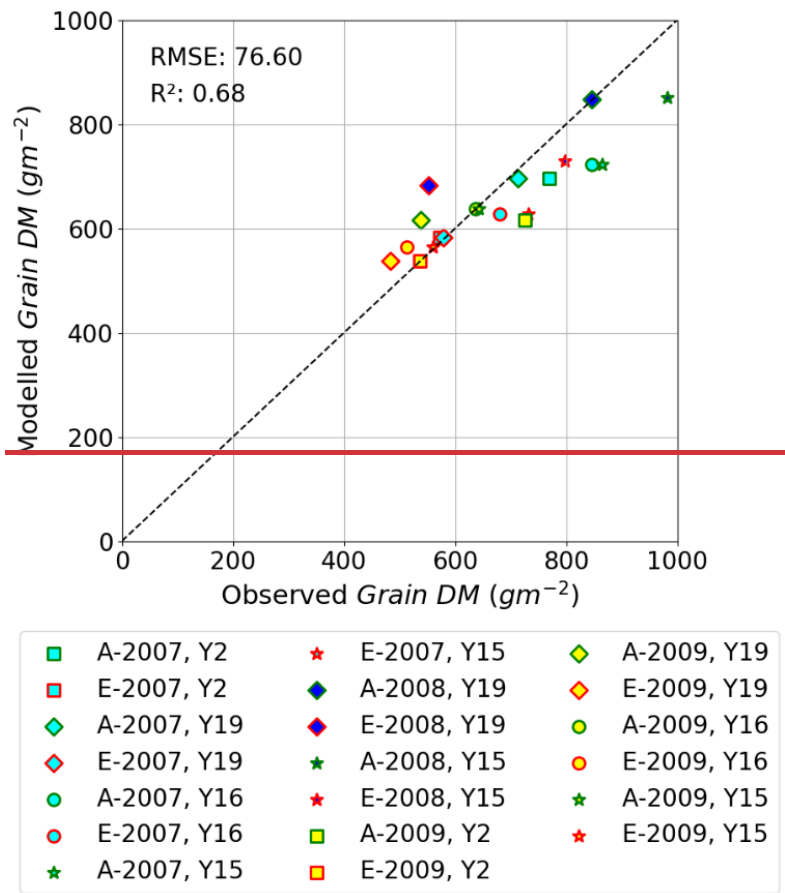
b).



821

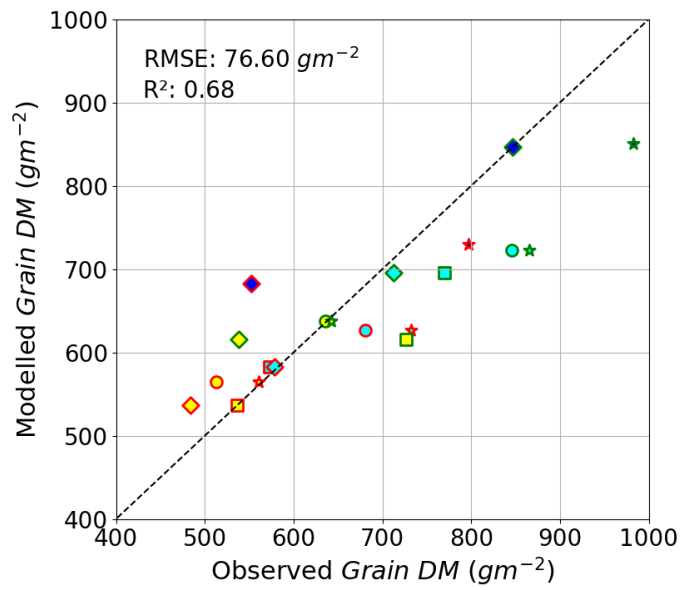
822 Finally, Fig 9 shows the relationship between modelled vs observed *Grain DM* (in  $\text{g m}^{-2}$ ) as a scatter  
 823 plot, a linear regression through these data gives an  $R^2$  value of 0.68 and RMSE of  $76 \text{ g m}^{-2}$ , showing  
 824 the model is able to simulate with reasonable accuracy the differences in absolute yield for different  
 825 cultivars and for different years. There are some instances of both underestimation and  
 826 overestimation, however the deviations from the 1:1 line is not excessively large. These model test  
 827 results compare with an  $R^2$  of 0.92 ( $n=4$ ) and an RMSE of  $25.49 \text{ g m}^{-2}$  for the training dataset (Y2 and  
 828 Y16 cultivar and year 2008, see Figure S3), the stronger agreement between observed and modelled  
 829 training dataset, as well as the reasonable agreement for the entire dataset would suggest the  
 830 model is not over-fitted. We find that we tend to underestimate the  $\text{O}_3$ -induced relative yield loss  
 831 (RYL) by between -2.76 and 15.34 (observed less modelled RYL) across all years and cultivars.

832 Fig. 9. A scatter plot showing modelled vs observed *Grain DM* (in  $\text{g m}^{-2}$ ) for the AA and E O<sub>3</sub>  
 833 treatments for all 4 cultivars and 3 years of the Xiaoji dataset; these data include those used for  
 834 evaluation.



835

836



■	A-2007, Y2	★	E-2007, Y15	◆	A-2009, Y19
□	E-2007, Y2	◆	A-2008, Y19	◇	E-2009, Y19
◇	A-2007, Y19	◆	E-2008, Y19	●	A-2009, Y16
◇	E-2007, Y19	★	A-2008, Y15	○	E-2009, Y16
●	A-2007, Y16	★	E-2008, Y15	★	A-2009, Y15
○	E-2007, Y16	■	A-2009, Y2	★	E-2009, Y15
★	A-2007, Y15	□	E-2009, Y2		

837

## 838 Discussion

839 The DO<sub>3</sub>SE-Crop model was found capable of simulating O<sub>3</sub> damage to grain yield for O<sub>3</sub>-FACE  
840 conditions at the experimental site in Xiaoji, China with a good degree of accuracy. Simulated  
841 relative yield losses (RYLs) between AA and E O<sub>3</sub> treatments for all years ranged between 11 to 14%  
842 and 13 to 19% for tolerant and sensitive cultivars respectively, these tend to be lower (particularly  
843 for the more extreme O<sub>3</sub> induced yield losses of the sensitive cultivars) than the observed values of  
844 13 to 20% and 10 to 35%. Overall, simulations of tolerant and sensitive cultivars underestimated  
845 RYLs by 4% and 7% respectively on average across years and cultivars (see data in section S6). This  
846 would suggest that O<sub>3</sub>-induced yield losses can be more reliably modelled for tolerant cultivars,  
847 possibly because additional processes causing O<sub>3</sub>-induced yield losses in sensitive cultivars are not  
848 captured. Such processes might include the effect of O<sub>3</sub> on the allocation of carbon to different plant  
849 parts (Feng et al., 2008) or O<sub>3</sub> inducing additional respiratory costs *via* the upregulation of defence  
850 mechanisms (Biswas et al., 2008). The model was also able to simulate absolute  
851 *Grain DM* reasonably well. Under AA O<sub>3</sub> levels *Grain DM* simulated for all years and cultivars were  
852 between 616 and 851 g/m<sup>2</sup> compared to observations of between 537 and 982 g/m<sup>2</sup>. There is a  
853 tendency to overestimate *Grain DM* under ambient conditions and underestimate *Grain DM* under  
854 elevated O<sub>3</sub> which is reflected in the RYL values.

855 Overall, the DO<sub>3</sub>SE-Crop model simulation results compare favourably to results made by the  
856 MCWLA-Wheat model (Tao et al., 2017) which was also calibrated for the Xiaoji experimental  
857 conditions but without distinction between tolerant and sensitive varieties. MCWLA-Wheat  
858 simulations of absolute yield varied between ~5700 and 9000 kg/ha (compared to ~5700 to 9800  
859 kg/ha) for ambient and ~4800 to 8000 kg/ha (compared to ~5200 to 8000 kg/ha) for elevated O<sub>3</sub>  
860 treatments. A mean relative yield loss of 14% was simulated by the model.

861 It is useful to set these site-specific estimates of O<sub>3</sub>-induced yield losses in the context of yield losses  
862 estimated using more traditional, concentration based O<sub>3</sub> risk assessment methods. A seminal paper  
863 by Feng et al. (2022) estimated mean relative yield losses across East Asia due to ambient O<sub>3</sub>  
864 concentrations at 33% (with a mean range of 28 to 37%) according to a mean monitored O<sub>3</sub>  
865 concentrations of 30.9 ppm h expressed as AOT40 (six-month accumulated daytime O<sub>3</sub>  
866 concentration above a threshold of 40 ppb). The mean difference in AOT40 (accumulated over only  
867 75 days) between the AA and E O<sub>3</sub> treatments at Xiaoji across all years was 7.8 ppm h giving a mean  
868 relative yield loss of approximately 10 to 20% depending on year and cultivar. As such, our modelled  
869 results in terms of RYLs between AA and E O<sub>3</sub> treatments are consistent with these broader results  
870 for East Asia.

871 Crop phenology plays a crucial role in determining the timing of the important O<sub>3</sub> exposure period  
872 (i.e., from anthesis to maturity), and hence O<sub>3</sub> damage. Evaluation of the DO<sub>3</sub>SE-crop phenology  
873 model shows the model is able to accurately simulate crop phenology for the three years at Xiaoji (R<sup>2</sup>  
874 =0.95 and RMSE =2.5, see Fig. 3). Estimating the correct timing of anthesis is crucial since the period  
875 from anthesis to crop maturity is the O<sub>3</sub>-sensitive period. During this period, accumulated stomatal  
876 O<sub>3</sub> flux ( $acc_{fst}$ ) will contribute to early and enhanced senescence once the critical threshold  
877 ( $CLsO3$ ) is exceeded. This period also coincides with carbon accumulation in the grain (Kohut et al.,  
878 1987; Feng et al., 2008) which may be limited by O<sub>3</sub>-induced early onset or enhanced senescence.  
879 The DO<sub>3</sub>SE-crop model was developed to accommodate the full range of effects of O<sub>3</sub> on senescence  
880 with revised functions, similar to those first developed by Ewert and Porter (2000), able to modify  
881 both the O<sub>3</sub> induced onset of senescence as well as the O<sub>3</sub> effect on maturity. This is important since  
882 experimental evidence has shown that O<sub>3</sub> can bring forward the maturity date; for example, the flag



883 leaf was found to have senesced 25 days earlier in a high O<sub>3</sub> treatment, compared to a charcoal-  
884 filtered treatment (Grandjean and Fuhrer, 1989; Gelang et al., 2000). O<sub>3</sub> was also found to cause  
885 differences in the time to maturity of the flag leaf, with Shi et al. (2009) reporting that maturity was  
886 brought forward by 8 days under an elevated O<sub>3</sub> treatment (50% higher than ambient). Currently,  
887 other crop models with O<sub>3</sub> damage functions (e.g. MLCWLA-Wheat (Tao et al., 2017) and LINTULLCC-  
888 2 (Feng et al., 2022) are only able to bring the O<sub>3</sub>-induced onset of senescence earlier.

889 The DO<sub>3</sub>SE-crop model is also able to simulate differential O<sub>3</sub> uptake in each canopy layer. Fig. 5  
890 shows that the majority of stomatal O<sub>3</sub> uptake occurs in the sunlit layers of the upper canopy. Similar  
891 results were found in an experimental study on a productive grassland in Switzerland (Jaggi et al.,  
892 2006) who found that different levels of O<sub>3</sub> exposure to canopy components predominantly located  
893 in the upper and lower parts of the canopy support a multi-layer approach to modelling O<sub>3</sub> uptake.  
894 Therefore, the focus on the upper canopy by flux-based O<sub>3</sub> metrics (e.g. the phytotoxic ozone dose  
895  $POD_y$ , (UNECE, 2017) seems rational in the absence of multi-layer modelling. Crop models such as  
896 LINTULCC-2 (Feng et al., 2022) also focus on estimating stomatal O<sub>3</sub> uptake at the top of the canopy  
897 to estimate O<sub>3</sub> induced yield losses. For wheat, such an approach is further supported by the fact  
898 that the upper canopy layers consist of the flag leaf, which plays a crucial role in photosynthesis and  
899 grain filling (Pleijel et al., 2007). The multi-layer functionality of the DO<sub>3</sub>SE-Crop model may however  
900 become more useful when considering crops that partition assimilated carbon to harvest organs  
901 earlier in their growing season such as potato (Okrah et al. 2023).

902 Our results show that the DO<sub>3</sub>SE-crop model was able to estimate the seasonal course of leaf  $A_{net}$   
903 and  $g_{O_3}$  daily maxima observed at the Xiaoji site (see Fig. 4a) and when compared to other literature  
904 describing leaf physiological variables (Guan et al., 2015; Li et al., 2022). This suggests the coupled  
905  $A_{net}g_{sto}$  model is working for Chinese conditions (having previously been applied and evaluated for  
906 European O<sub>3</sub> experimental conditions – see Pande et al., 2024). The leaf physiology parameters used  
907 in this study (i.e. for Asian conditions and cultivars) are higher than parameters for European studies.  
908 For Europe,  $V_{cmax}$  values of between 60 and 90  $\mu\text{mol CO}_2 \text{ m}^{-2} \text{ s}^{-1}$  were found in the literature (Feng  
909 et al., 2022; Pande et.al., 2024, Van Oijen and Ewert, 1999) compared to the observed mean  
910 maximum value of 137  $\mu\text{mol CO}_2 \text{ m}^{-2} \text{ s}^{-1}$  at Xiaoji which was used in this study. Similarly, European  
911  $J_{max}$  values ranged from 160 to 180  $\mu\text{mol CO}_2 \text{ m}^{-2} \text{ s}^{-1}$  (Feng et al., 2021, Pande et al. 2024, Van Oijen  
912 & Ewert, 1999) compared to the observed Xiaoji mean maximum value of 228  $\mu\text{mol CO}_2 \text{ m}^{-2} \text{ s}^{-1}$ . Even  
913 though these leaf physiology parameters are higher, absolute yields for these Chinese cultivars are  
914 consistent with those found under European conditions. This most likely reflects the importance of  
915 other environmental conditions (e.g., high vapour pressure deficits) limiting leaf carbon assimilation.  
916 Moreover, the complex interactions between O<sub>3</sub> exposure and the plants' physiological responses  
917 also play a crucial role. Ozone significantly affected antioxidative enzymes, thereby limiting overall  
918 photosynthetic efficiency and yield, particularly in O<sub>3</sub>-sensitive cultivars, despite their ability to  
919 maintain high carboxylation capacity.

920 Ensuring the seasonal variation in carbon allocation to the different components of the crop (i.e.,  
921 roots, stem, leaves and harvest organs) is essential for the simulation of crop growth and yield.  
922 There are limited data in the literature that provide these variables, so we compare our results to  
923 the carbon allocation profiles described for wheat provided in the original JULES Crop model  
924 description, recognising this is intended for wheat grown globally. The DO<sub>3</sub>SE-Crop model carbon  
925 allocation to the stem and roots is comparatively higher than was simulated by JULES Crop (Osborne  
926 et al., 2015; see Fig. 6a). However, we can justify the carbon allocation coefficients used for Xiaoji  
927 since the DO<sub>3</sub>SE-Crop model was able to distribute carbon to different plant components to produce  
928 a well-proportioned plant over the course of the growing season, this was determined by the  
929 calibration to a number of key crop variables (i.e., ratios of plant respiration,  $LAI$ , stem to leaf dry

930 matter, above ground components and grain dry matter). Importantly, when applied to the test  
931 dataset (i.e. excluding 2008 data for the Y2 and Y16 cultivar), the model, was found to simulate the  
932 grain dry matter under ambient and elevated O<sub>3</sub> treatments to within 7.9-8.7% of the observed  
933 values (R<sup>2</sup> =0.68, 76 g/m<sup>2</sup> see Fig. 9).

934 The DO<sub>3</sub>SE-Crop model, similar to other crop models with O<sub>3</sub> damage functions (i.e. MLCWLA-Wheat  
935 (Tao *et al.*, 2017) and LINTULLCC-2 (Feng *et al.*, 2022), [WOFOST \(Nguyen et al., 2024\)](#)) has the  
936 capacity to simulate both the instantaneous and long-term O<sub>3</sub> impact on wheat grain yield. The  
937 instantaneous O<sub>3</sub> effect on photosynthesis may cause leaf cell damage and decrease the supply of  
938 carbohydrate precursors which can significantly decrease  $g_{O_3}$ ,  $V_{cmax}$  and leaf chlorophyll content  
939 (Farage *et al.*, 1991). Elevated O<sub>3</sub> also leads to generation of reactive oxygen species (ROS) in plant  
940 cells which can cause oxidative damage to various cellular components. Rubisco, the enzyme  
941 responsible for carbon fixation in the photosynthetic process, can be particularly susceptible to this  
942 damage, leading to a reduced carboxylation rate ( $V_{cmax}$ ). Such an O<sub>3</sub> effect on  $V_{cmax}$  reduces net  
943 photosynthesis and can also induce early senescence shortening the grain filling period (Triboi and  
944 Triboi-Blondel, 2002).

945 Results from the DO<sub>3</sub>SE-crop model found a larger impact on yield due to the long-term O<sub>3</sub> impact  
946 causing relative yield loss of between 10 to 31% compared to only 0 to 0.2% resulting from the  
947 instantaneous O<sub>3</sub> impact on photosynthesis. Previous studies have also found that the long-term O<sub>3</sub>  
948 effect has a larger impact on yield compared to the instantaneous effect of O<sub>3</sub> on photosynthesis  
949 (Emberson *et al.*, 2018; Brewster *et al.*, 2024). Senescence is an age-dependent process of  
950 degradation and degeneration that allows nutrients to be re-distributed to different plant organs  
951 (Lim *et al.*, 2007). Under O<sub>3</sub> stress, this process is often found to occur earlier and more rapidly in  
952 leaves as well as at the whole plant or crop canopy scale (Brewster *et al.*, 2024). The causes of this  
953 early and accelerated senescence are not completely understood but may be related to O<sub>3</sub> induced  
954 enhanced expression of many genes involved in natural senescence (Miller *et al.*, 1999). Elevated O<sub>3</sub>  
955 was also found to inhibit sugar export from leaves (Singh Yadav *et al.*, 2020; Feng *et al.*, 2024) which  
956 could trigger early onset of leaf senescence.

957 The DO<sub>3</sub>SE-crop model accounts for the impact of O<sub>3</sub> on the Rubisco enzyme by incorporating  
958 modified (Ewert and Porter, 2000) functions for instantaneous and long-term O<sub>3</sub> impact on  $V_{cmax}$  as  
959 an important parameter used to characterize the crop photosynthetic capacity (Ewert and Porter,  
960 2000; Osborne *et al.*, 2019). The DO<sub>3</sub>SE-crop model assumes that the O<sub>3</sub> will only accumulate on  
961 exceedance of a stomatal O<sub>3</sub> flux threshold of 6 nmol O<sub>3</sub> m<sup>-2</sup> s<sup>-1</sup>. The long-term O<sub>3</sub> impact mechanism  
962 of the DO<sub>3</sub>SE-crop model simulated the effect of senescence on  $V_{cmax}$  reasonably well as evidenced  
963 by the reduction in leaf chlorophyll content. We used the breakpoint method (Yang *et al.*, 2016;  
964 Mariën *et al.*, 2019) to estimate the SOS and EOS using the day of the year and measured  
965 chlorophyll content (Fig. 7 and Fig. S4). It is crucial to accurately model the timing of SOS and EOS  
966 correctly as this determines the O<sub>3</sub> effect on the duration of the grain filling period and hence the  
967 difference in yield loss due to different O<sub>3</sub> treatments. For example, we modelled a difference of 3 to  
968 5 in SOS, and 6 to 9 days in EOS, on average across years for the sensitive and tolerant cultivar  
969 respectively.

970 China's wheat breeding programme has seen more than 1,850 varieties used across China between  
971 the 1920s to 2014 leading to increased yields from less than 1 to more than 5 tonnes ha<sup>-1</sup> (Qin *et al.*,  
972 2015). Here, albeit with an extremely limited dataset, we parameterise the DO<sub>3</sub>SE-crop model for  
973 tolerant and sensitive wheat crop cultivars, since many experimental studies have shown that the  
974 response of different cultivars to O<sub>3</sub> stress differs (Biswas *et al.*, 2008). Based on the available data  
975 the model seemed able to capture the difference in grain dry matter between these different  
976 cultivar groups across different years reasonably well when compared to the observed dataset (R<sup>2</sup>

977 =0.68; see Fig. 8). Such a cultivar sensitivity-based parametrisation can provide additional  
978 information on the certainty of regional yield loss estimates given the large number of wheat  
979 varieties grown across China. However, when applying the model to a broader region, it would be  
980 advisable to calibrate phenology for different agro-ecological zones as the temperature changes  
981 across China, impacting the duration of the key phenological stages such as anthesis and maturity  
982 (Luo et.al., 2021). Additionally, carbon allocation parameters may need adjustment, as studies have  
983 shown changes in dry matter content across different agro-ecological zones (Hussain and Bagash,  
984 2017).

985 **Conclusions**

986 We have shown that the newly developed DO<sub>3</sub>SE-Crop model can be calibrated for O<sub>3</sub> tolerant and  
987 sensitive wheat varieties for O<sub>3</sub>-FACE site conditions at Xioaji in China. The model can simulate crop  
988 phenology, leaf physiology, crop growth and yield reasonably well across different years. The model  
989 is also able to simulate the effect of O<sub>3</sub> stress on grain yield distinguishing the extent of O<sub>3</sub> damage  
990 resulting from the same O<sub>3</sub> treatment on cultivars with differing O<sub>3</sub> sensitivities. The DO<sub>3</sub>SE-Crop  
991 model also has the advantage of simulating O<sub>3</sub> transfer and deposition dynamics within the wheat  
992 crop canopy which could in the future improve our understanding of whole canopy O<sub>3</sub> effects for  
993 crops with different carbon allocation profiles. The ability of the model to estimate relative yield  
994 losses across years also suggests the model is 'fit for purpose' to assess the effects of O<sub>3</sub> under a  
995 variety of climate variable and O<sub>3</sub> concentration conditions.

## Appendix A

### A1. DO<sub>3</sub>SE-Crop variables

Variable	Unit	Description
$T_{eff}$	°C days	Effective temperature accumulated between sowing to maturity
$DVI$	-	Development index
$T_{air}$	°C	Surface air temperature in degrees Celsius
$T_{air,k}$	degrees Kelvin	Surface air temperature in Kelvin
$T_{min}$	°C	Daily minimum surface air temperature
$T_{max}$	°C	Daily maximum surface air temperature
$LTT$	°C d	Thermal time accumulated by a leaf
$V_{dd}$	days	Accumulated vernalised days
$V$	days	Vernalised days
$V_d$	days	Devernalised days
$VF$	-	Vernalisation factor
$PP$	hrs	Photoperiod
$PF$	-	Photoperiod factor
$A_{net}$	$\mu\text{mol CO}_2 \text{ m}^{-2} \text{ s}^{-1}$	Net photosynthesis or rate of CO <sub>2</sub> assimilation
$A_c$	$\mu\text{mol CO}_2 \text{ m}^{-2} \text{ s}^{-1}$	RuBP (ribulose-1,5-bisphosphate) limited $A_{net}$
$A_j$	$\mu\text{mol CO}_2 \text{ m}^{-2} \text{ s}^{-1}$	Electron transport limited $A_{net}$
$A_p$	$\mu\text{mol CO}_2 \text{ m}^{-2} \text{ s}^{-1}$	TPU (triose phosphate) limited $A_{net}$
$R_d$	$\mu\text{mol CO}_2 \text{ m}^{-2} \text{ s}^{-1}$	Dark respiration
$f_{PAW}$	-	Fraction of plant available water
$PAW_t$	-	Threshold of PAW, above which $g_{sto}$ is at a maximum as described $f_{PAW}$ function
$PAW$	$\text{m}^3/\text{m}^3$	Plant available water
$C_i$	$\mu\text{mol}/\text{mol}$	Intercellular CO <sub>2</sub> partial pressure
$O_i$	$\text{mmol}/\text{mol}$	Intercellular O <sub>2</sub> concentrations
$\Gamma^*$	$\mu\text{mol}/\text{mol}$	CO <sub>2</sub> compensation point in the absence of respiration
$\Gamma$	$\mu\text{mol}/\text{mol}$	CO <sub>2</sub> compensation point
$J$	$\mu\text{mol CO}_2 \text{ m}^{-2} \text{ s}^{-1}$	electron transport rate
$VPD$	kPa	Leaf to air vapour pressure deficit
$C_z$	ppb	O <sub>3</sub> concentration at reference height $z$
$C_h$	$\text{nmol}/\text{m}^3$	O <sub>3</sub> concentration at the crop canopy height
$C_{zh}$	$\text{nmol}/\text{m}^3$	O <sub>3</sub> concentration at the top of the crop canopy height
$C_{zb}$	$\text{nmol}/\text{m}^3$	O <sub>3</sub> concentration at the bottom of the crop canopy height
$f_{st}$	$\text{nmol O}_3 \text{ m}^{-2} \text{ s}^{-1}$	Leaf level stomatal O <sub>3</sub> flux
$accf_{st}$	$\text{mmol O}_3 \text{ m}^{-2}$	Accumulated stomatal O <sub>3</sub> flux
$C_l$	$\text{nmol O}_3 \text{ m}^{-3}$	O <sub>3</sub> at the upper surface of the laminar layer of a leaf

$f_{O_3,s}(d)$	-	Effect of daily cumulative stomatal $O_3$ flux on $V_{c_{max}}$
$f_{O_3,s}(h)$	-	Effect of hourly cumulative stomatal $O_3$ flux on $V_{c_{max}}$
$f_{O_3,s}(d - 1)$	-	Previous days effect of cumulative stomatal $O_3$ flux on $V_{c_{max}}$
$r_{O_3,s}$	-	Incomplete overnight recovery of $O_3$ affected $V_{c_{max}}$
$f_{LA}$	-	Leaf age related capacity to recover from accumulated stomatal $O_3$ flux
$f_{O_3}$	-	Weighted accumulated stomatal $O_3$ flux that determines the onset of leaf senescence
$f_{LS}$	-	Accumulated stomatal $O_3$ flux effect on leaf senescence
$tl$	°C days	Effective temperature accumulated by a leaf after emergence ( $DVI = 0$ )
$tl_{ep}$	-	Effective temperature accumulated by a leaf between full expansion and the onset of leaf senescence
$tl_{epO_3}$	-	Effective temperature accumulated by a leaf between full expansion and the onset of leaf senescence brought forward by $O_3$
$tl_{se}$	-	Effective temperature accumulated by a leaf between the onset of leaf senescence and maturity
$tl_{seO_3}$	-	Effective temperature accumulated by a leaf between the onset of leaf senescence and maturity brought forward by $O_3$
$g_{CO_2}$	$\mu\text{mol CO}_2 \text{ PLA m}^{-2} \text{ s}^{-1}$	Stomatal conductance to $\text{CO}_2$
$f_{VPD}$	-	Relationship between VPD and relative stomatal conductance
$c_s$	$\text{mol CO}_2/\text{mol}$	External $\text{CO}_2$ concentration at the leaf surface
$c_a$	$\text{mmol CO}_2/\text{mol}$	external $\text{CO}_2$ concentration at the upper surface of the leaf boundary layer
$g_{bCO_2}$	$\text{mol m}^{-2} \text{ s}^{-1}$	Quasi laminar boundary layer conductance to $\text{CO}_2$
$C_z$	$\text{nmol O}_3 \text{ m}^{-3}$	$O_3$ concentration at reference height ( $z$ )
$C_l$	$\text{nmol O}_3 \text{ m}^{-3}$	$O_3$ concentration at the upper surface of the laminar layer of a leaf
$g_{O_3}$	$\text{mmol O}_3 \text{ PLA m}^{-2} \text{ s}^{-1}$	Stomatal conductance to $O_3$
$g_{O_3m/s}$	$\text{m/s}$	Stomatal conductance to $O_3$
$g_{ext}$	$\text{m/s}$	External conductance
$r_c$	$\text{s/m}$	Leaf surface resistance to $O_3$
$r_{b,O_3}$	$\text{s/m}$	Quasi laminar leaf boundary layer resistance to $O_3$
$r_a$	$\text{s/m}$	Atmospheric resistance to $O_3$
$r_{inc}$	$\text{s/m}$	In-canopy resistance to $O_3$
$r_{ext}$	$\text{s/m}$	External plant cuticle resistance to $O_3$
$r_{sto}$	$\text{s/m}$	Stomatal resistance to $O_3$
$u_z$	$\text{m/s}$	Wind speed at a reference height $z$
$u_l$	$\text{m/s}$	Wind speed at the upper surface of the laminar layer of a leaf
$L$	$\text{m}$	Cross wind leaf dimension
$LAI$	$\text{m}^2 \text{ m}^{-2}$	Leaf Area Index
$PAR_{dir,i}$	$\text{W/m}^2$	Direct PAR in canopy layer $i$
$PAR_{diff,i}$	$\text{W/m}^2$	Diffuse PAR in canopy layer $i$
$PAR_{total}$	$\text{W/m}^2$	Direct and diffuse PAR at the top of the canopy

$NPP$	kg C m <sup>-2</sup>	Net primary productivity
$GPP$	kg C m <sup>-2</sup>	Gross primary productivity
$R_p$	kg C m <sup>-2</sup>	Plant respiration
$R_{pm}$	kg C m <sup>-2</sup>	Plant maintenance respiration
$R_{pg}$	kg C m <sup>-2</sup>	Plant growth respiration
$A_{netc}$	kg C m <sup>-2</sup>	Canopy net photosynthesis
$R_{dc}$	kg C m <sup>-2</sup>	Non-water stressed canopy dark respiration
$f_{sw}R_{dc}$	kg C m <sup>-2</sup>	Water stressed modified canopy dark respiration
$C_{root}$	kg C m <sup>-2</sup>	Root C pool
$C_{leaf}$	kg C m <sup>-2</sup>	Leaf C pool
$C_{stem}$	kg C m <sup>-2</sup>	Stem C pool
$C_{resv}$	kg C m <sup>-2</sup>	Reserve C pool
$C_{harv}$	kg C m <sup>-2</sup>	Harvest pool
$P_{root}$	-	Root C pool partition coefficient
$P_{leaf}$	-	Leaf C pool partition coefficient
$P_{stem}$	-	Stem C pool partition coefficient
$P_{resv}$	-	Reserve C pool partition coefficient
$P_{harv}$	-	Harvest C pool partition coefficient
$C_{leaf,green}$	kg C m <sup>-2</sup>	Green leaf C
$C_{leaf,brown}$	kg C m <sup>-2</sup>	Brown leaf C
$SLA$	m <sup>2</sup> kg <sup>-1</sup>	Specific Leaf Area
$h$	m	Crop height
$Yield_{grain}$	g C m <sup>-2</sup>	Grain yield
$k_p'$	-	Beam and scattered beam PAR extinction coefficient
$k_d'$	-	Diffuse and scattered diffuse PAR extinction coefficient
$\rho_{cb}$	-	Canopy reflection coefficient for beam PAR
$\rho_{cd}$	-	Canopy reflection coefficient for diffuse PAR
$\beta$	Radians	Solar elevation angle
$\delta$	Radians	Solar declination angle
$PAR_{dir} (LAI)$	$\mu\text{mol m}^{-2} \text{s}^{-1}$	Absorbed beam plus scattered beam PAR per unit leaf area
$PAR_{diff} (LAI)$	$\mu\text{mol m}^{-2} \text{s}^{-1}$	Absorbed diffuse plus scattered diffuse PAR per unit leaf area
$PAR (LAI)$	$\mu\text{mol m}^{-2} \text{s}^{-1}$	Total absorbed PAR per unit leaf area
$I_b (LAI)$	$\mu\text{mol m}^{-2} \text{s}^{-1}$	Direct PAR per unit ground area
$I_d (LAI)$	$\mu\text{mol m}^{-2} \text{s}^{-1}$	Diffuse PAR per unit ground area
$I_d (0)$	$\mu\text{mol m}^{-2} \text{s}^{-1}$	Diffuse PAR per unit ground area at the top of the canopy
$I_b (0)$	$\mu\text{mol m}^{-2} \text{s}^{-1}$	Beam PAR per unit ground area at the top of the canopy
$PAR_{ps} (LAI)$	$\mu\text{mol m}^{-2} \text{s}^{-1}$	Absorbed scattered beam PAR per unit leaf area
$PAR_{psun} (LAI)$	$\mu\text{mol m}^{-2} \text{s}^{-1}$	Beam PAR absorbed by sunlit leaves per unit leaf area

$PAR_{sh}$ (LAI)	$\mu mol m^{-2} s^{-1}$	Beam PAR absorbed byshaded leaves per unit leaf area
$PAR_{sun}$ (LAI)	$\mu mol m^{-2} s^{-1}$	Total PAR absorbed by sunlit leaves per unit leaf area
$PAR_{total}$	$\mu mol m^{-2} s^{-1}$	Total absorbed irradiance per unit leaf area
LAI	$m^2 m^{-2}$	Cumulative leaf area index from top of canopy (L=0 at top)
$f_{1,2}$ (LAI)	-	Fraction of leaf area in a leaf-angle class
LAI <sub>sh</sub>	-	Fraction of leaves that are shaded
LAI <sub>sun</sub>	-	Fraction of leaves that are sunlit
$\sigma$	-	Leaf scattering coefficient for PAR
$\alpha_1$	Radians	Angle of beam irradiance to the leaf normal
$\sin\beta$	-	Solar elevation angle
$k_b'$	-	Beam and scattered beam PAR extinction coefficient
$k_d'$	-	Diffuse and scattered diffuse PAR extinction coefficient
$\sigma$	-	Leaf scattering coefficient for PAR
$\alpha_1$	Radians	Angle of beam irradiance to the leaf normal

A2. DO<sub>3</sub>SE-Crop parameters for wheat. Highlighted are the parameters (and their associated ranges) which require calibration when applying DO<sub>3</sub>SE-Crop to varying environmental conditions.

Parameter	Unit	Default Value	Description	Reference	Range	Calibrated Parameter Value
$T_b$	°C	0	Base temperature	(Tao, Zhang and Zhang, 2012; Osborne <i>et al.</i> , 2015)	-0.5-1	-0.25
$T_o$	°C	20	Optimum temperature	(Tao, Zhang and Zhang, 2012; Osborne <i>et al.</i> , 2015)	15-25	17.79
$T_m$	°C	30	Maximum temperature	(Tao, Zhang and Zhang, 2012; Osborne <i>et al.</i> , 2015)	25-40	23.87
$TT_{emr}$	°C d	100	Thermal time between sowing and emergence	(Lu <i>et al.</i> , 2018; Luo <i>et al.</i> , 2020)	50-100	220.6
$TT_{veg}$	°C d	940	Thermal time between emergence and anthesis	Xiaoji experimental dataset	400-940	940
$TT_{rep}$	°C d	304	Thermal time between anthesis and maturity	(Wang <i>et al.</i> , 2013a); Xiaoji experimental dataset	300-650	304
$TT_{leaf}$	°C d	1000	Total canopy-leaf life span of the crop, covers period from emergence to maturity, distributed over the DVI between 0 and 2	(Lu <i>et al.</i> , 2018; Luo <i>et al.</i> , 2020)	700-1200	795



$T_l$	°C d	1400	Total lifespan of the crop, covers the full period from sowing to maturity, corresponding to DVI between -1 to 2	(Ewert and Porter, 2000; Lu <i>et al.</i> , 2018; Luo <i>et al.</i> , 2020)	1300-1500	Year 2007- 1325, Year 2008- 1400, Year 2009- 1478.
$PIV$		1.5	Vernalisation coefficient	(Tao, Zhang and Zhang, 2012; Wang <i>et al.</i> , 2013)	2.9-4	2.9
$PID$		40	Photoperiod coefficient	(Wang <i>et al.</i> , 2013; Liu <i>et al.</i> , 2016; Zhao <i>et al.</i> , 2020)	40-57	40
$VT_{max}$	°C	30	Maximum daily temperature for vernalisation	Zheng <i>et al.</i> , 2015		
$VT_{min}$	°C	15	Minimum daily temperature for vernalisation	Zheng <i>et al.</i> , 2015		
$PAW_t$	m <sup>3</sup> /m <sup>3</sup>	50	Plant available soil water below which stomatal conductance will start to reduce	LRTAP, 2017		
$V_{cmax}$	µmol CO <sub>2</sub> m <sup>-2</sup> s <sup>-1</sup>	90	Maximum carboxylation capacity at 25°C	(Büker <i>et al.</i> , 2012)	90-140	137
$J_{max}$	µmol CO <sub>2</sub> m <sup>-2</sup> s <sup>-1</sup>	180	Maximum rate of electron transport at 25°C	(Büker <i>et al.</i> , 2012)	180-250	228
$K_c$	µmol/mol	404.9	Rubisco Michaelis-Menten constants for CO <sub>2</sub>	(Medlyn <i>et al.</i> , 2002)		
$K_0$	mmol/mol	278.4	Rubisco Michaelis-Menten constants for O <sub>2</sub>	(Medlyn <i>et al.</i> , 2002)		
$\Gamma^*$	µmol/mol	42.75	CO <sub>2</sub> compensation point in the absence of respiration	(Medlyn <i>et al.</i> , 2002)		
$a$	-	4	Electron requirement for the formation of NADPH	(Sharkey <i>et al.</i> , 2007)		
$b$	-	8	Electron requirement for the formation of ATP	(Sharkey <i>et al.</i> , 2007)		
$R_{dcoeff}$	-	0.015	Leaf dark respiration coefficient	(Clark <i>et al.</i> , 2011)	0.010-0.03	0.01
$f_{min}$	µmol CO <sub>2</sub> /m <sup>2</sup> /s	1000	Minimum daytime stomatal conductance to CO <sub>2</sub>	(Ewert and Porter, 2000)		
$m$	-	7	composite sensitivity slope constant	(Büker <i>et al.</i> , 2012)	4-15	5
$VPD_0$	kPa	2.2	stomatal conductance sensitivity to $VPD$	UNECE, 2017; Pande <i>et al.</i> 2024		
$\gamma_1$	-	0.027	O <sub>3</sub> short-term damage co-efficient	(Ewert and Porter, 2000)		
$\gamma_2$	(nmol O <sub>3</sub> m <sup>-2</sup> s <sup>-1</sup> ) <sup>-1</sup>	0.0045	O <sub>3</sub> short-term damage co-efficient	(Ewert and Porter, 2000)		
$\gamma_3$	(µmol O <sub>3</sub> m <sup>-2</sup> ) <sup>-1</sup>	0.00005	O <sub>3</sub> long-term damage co-efficient	(Ewert and Porter, 2000)	0.00001-0.00009	Tolerant=0.00001 Sensitive=0.00002

$\gamma_4$	-	5	O <sub>3</sub> long-term damage co-efficient determining onset of senescence		5-15	Tolerant=5 Sensitive=15
$\gamma_5$	-	0.8	O <sub>3</sub> long-term damage co-efficient determining maturity		0.5-5	Tolerant=0.8 Sensitive=5
$CLsO_3$	mmol O <sub>3</sub> m <sup>-2</sup>	6.5-20.6,20.5	Critical accumulated stomatal O <sub>3</sub> flux that determines the onset of leaf senescence	(Osborne <i>et al.</i> , 2019; Feng <i>et al.</i> , 2022)	3-21	4.2
$r_{ext}$	m/s	2500	External leaf cuticular resistance to O <sub>3</sub> uptake	UNECE, 2017		
$L$	m	0.02	Cross wind leaf dimension for wheat	UNECE, 2017		
$P_{st}$	Pa	1.013 x 10 <sup>5</sup>	Standard air pressure at 20°C	UNECE, 2017		
$T_{st}$	°C	20	Standard temperature	UNECE, 2017		
$R$	J/mol/K	8.31447	Universal gas constant	UNECE, 2017		
$n_e$	mol CO <sub>2</sub> m <sup>-2</sup> s <sup>-1</sup> kg C (kg N) <sup>-1</sup>	0.0008	Constant relating leaf nitrogen to rubisco carboxylation capacity	(Clark <i>et al.</i> , 2011)		
$n_0$	kg N [kg C] <sup>-1</sup>	0.073	Top canopy leaf N concentration	(Clark <i>et al.</i> , 2011)		
$kN$		0.78	Nitrogen profile co-efficient	(Clark <i>et al.</i> , 2011)		
$R_{gcoeff}$	-	0.25	Plant growth respiration coefficient	(Osborne <i>et al.</i> , 2015)	0.15-0.25	0.16
$\alpha_{root}$	-	18.5	Coefficient for determining partitioning	(Osborne <i>et al.</i> , 2015)	16-19	18.4
$\alpha_{stem}$	-	16.0	Coefficient for determining partitioning	(Osborne <i>et al.</i> , 2015)	16-17	16.8
$\alpha_{leaf}$	-	18.0	Coefficient for determining partitioning	(Osborne <i>et al.</i> , 2015)	18-19	18.5
$\beta_{root}$	--	-20.0	Coefficient for determining partitioning	(Osborne <i>et al.</i> , 2015)	20-21	-20.9
$\beta_{stem}$	-	-15.0	Coefficient for determining partitioning	(Osborne <i>et al.</i> , 2015)	14-16	-14.5
$\beta_{leaf}$	-	-18.5	Coefficient for determining partitioning	(Osborne <i>et al.</i> , 2015)	18-19	-18.11
$f_c$	-	0.5	Carbon fraction of dry matter	(Osborne <i>et al.</i> , 2015)		
$\Upsilon$	m <sup>-2</sup> kg <sup>-1</sup>	27.3	Coefficient for determining specific leaf area	(Osborne <i>et al.</i> , 2015)	13-28	13.5
$\delta$	-	-0.0507	Coefficient for determining specific leaf area	(Osborne <i>et al.</i> , 2015)		
$k$	-	1.4	allometric coefficient which relates $C_{stem}$ to $h$	(Osborne <i>et al.</i> , 2015)		
$\tau$	-	0.4	allometric coefficient which relates $C_{stem}$ to $h$	(Osborne <i>et al.</i> , 2015)	0.3-0.6	0.4

$D_w$	-	1/0.84	Conversion factor to allow for grain moisture content	(Mulvaney and Devkota, 2020)		
$E_g$	-	0.85	Conversion factor for grain to ear ratio	(Nagarajan <i>et al.</i> , 1999; Kutman, Yildiz and Cakmak, 2011)		
$R_{SL}$	-	2:1	Stem dry matter to leaf dry matter ratio	(Huang et al., 2022)		
$k_b'$	-	$0.46/\sin\beta$	Beam and scattered beam PAR extinction coefficient	(Pury and Farquhar, 1997)		
$k_d'$	-	0.8	Diffuse and scattered diffuse PAR extinction coefficient	(Pury and Farquhar, 1997)		
$\sigma$	-	0.15	Leaf scattering coefficient for PAR	(Pury and Farquhar, 1997)		
$\alpha_1$	Radians	0.5	Angle of beam irradiance to the leaf normal	(Pury and Farquhar, 1997)		

## References

### References

Amthor, J. S., Bar-Even, A., Hanson, A. D., Millar, A. H., Stitt, M., Sweetlove, L. J., and Tyerman, S. D.: Engineering strategies to boost crop productivity by cutting respiratory carbon loss, *Plant Cell*, 31(2), 297–314, <https://doi.org/10.1105/tpc.18.00743>, 2019.

Betzelberger, A. M., Gillespie, K. M., McGrath, J. M., Koester, R. P., Nelson, R. L., and Ainsworth, E. A.: Ozone exposure response for U.S. soybean cultivars: Linear reductions in photosynthetic potential, biomass, and yield, *Plant Physiology*, American Society of Plant Biologists, 160(4), 1827–1839, <https://doi.org/10.1104/pp.112.205591>, 2012.

[Beven, K.: A manifesto for the equifinality thesis. \*Journal of Hydrology\*, 320\(1–2\), 18–36. https://doi.org/10.1016/j.jhydrol.2005.07.007, 2006.](https://doi.org/10.1016/j.jhydrol.2005.07.007)

Biswas, D. K., Xu, H., Li, Y. G., Sun, J. Z., Wang, X. Z., Han, X. G., and Jiang, G. M.: Assessing the genetic relatedness of higher ozone sensitivity of modern wheat to its wild and cultivated progenitors/relatives, *Journal of Experimental Botany*, 59(4), 951–963, <https://doi.org/10.1093/jxb/ern022>, 2008.

Brewster, C., Fenner, N., and Hayes, F.: Chronic ozone exposure affects nitrogen remobilization in wheat at key growth stages, *Science of The Total Environment*, Elsevier B.V., 908(August 2023), 168288, <https://doi.org/10.1016/j.scitotenv.2023.168288>, 2024.

Brewster, C., Hayes, F., and Fenner, N.: Ozone Tolerance Found in *Aegilops tauschii* and Primary Synthetic Hexaploid Wheat, *Plants*, 8(7), 195, <https://doi.org/10.3390/plants8070195>, 2019.

[Büker, P., Morrissey, T., Briolat, A., Falk, R., Simpson, D., Tuovinen, J.-P., Alonso, R., Barth, S., Baumgarten, M., Grulke, N., Karlsson, P. E., King, J., Lagergren, F., Matyssek, R., Nunn, A., Ogaya, R., Peñuelas, J., Rhea, L., Schaub, M., Uddling, J., Werner, W., and Emberson, L. D.: DO3SE modelling of soil moisture to determine ozone flux to forest trees, \*Atmospheric Chemistry and Physics\*, 12\(12\), 5537–5562, https://doi.org/10.5194/acp-12-5537-2012, 2012](https://doi.org/10.5194/acp-12-5537-2012)

Campbell, G. S., and Norman, J. M.: An introduction to Environmental Biophysics, Second Edition, Springer, 1998.

Challinor, A. J., Watson, J., Lobell, D. B., Howden, S. M., Smith, D. R., and Chhetri, N.: A meta-analysis of crop yield under climate change and adaptation, *Nature Climate Change*, 4(4), 287–291, <https://doi.org/10.1038/nclimate2153>, 2014.

Clark, D. B., Mercado, L. M., Sitch, S., Jones, C. D., Gedney, N., Best, M. J., Pryor, M., Rooney, G. G., Essery, R. L. H., Blyth, E., Boucher, O., Harding, R. J., Huntingford, C., and Cox, P. M.: The Joint UK Land Environment Simulator (JULES), model description – Part 2: Carbon fluxes and vegetation dynamics, *Geoscientific Model Development*, 4(3), 701–722, <https://doi.org/10.5194/gmd-4-701-2011>, 2011.

Conibear, L., Butt, E. W., Knote, C., Spracklen, D. V., and Arnold, S. R.: Current and Future Disease Burden From Ambient Ozone Exposure in India, *GeoHealth*, 2, 334–355, <https://doi.org/10.1029/2018GH000168>, 2018.

Danielsson, H., Karlsson, G. P., Karlsson, P. E., and Pleijel, H. H.: Ozone uptake modelling and flux-response relationships—an assessment of ozone-induced yield loss in spring wheat. *Atmospheric Environment*, 37(4), 475–485, [https://doi.org/10.1016/S1352-2310\(02\)00954-7](https://doi.org/10.1016/S1352-2310(02)00954-7), 2003.

Dentener, F., Emberson, L., Galmarini, S., Cappelli, G., Irimescu, A., Mihailescu, D., Van Dingenen, R., van den Berg, M.: Lower air pollution during COVID-19 lock-down: improving models and methods estimating ozone impacts on crops. *Philosophical Transactions of the Royal Society A: Mathematical, Physical and Engineering Sciences* 378, 20200188. <https://doi.org/10.1098/rsta.2020.0188>, 2020.

Droutsas, I., Challinor, A. J., Arnold, S. R., Mikkelsen, T. N., and Hansen, E. M. Ø.: A new model of ozone stress in wheat including grain yield loss and plant acclimation to the pollutant. *European Journal of Agronomy*, 120, 126125. <https://doi.org/10.1016/j.eja.2020.126125>, 2020.

Emberson, L. D., Ashmore, M. R., Simpson, D., Tuovinen, J.-P., and Cambridge, H. M.: Modelling and mapping ozone deposition in Europe, *Water, Air and Soil Pollution*, 577–582, 2001.

Emberson, L. D., Ashmore, M. R., Cambridge, H. M., Simpson, D., and Tuovinen, J.-P.: Modelling stomatal ozone flux across Europe, *Environmental Pollution*, 109(3), 403–413, [https://doi.org/10.1016/S0269-7491\(00\)00043-9](https://doi.org/10.1016/S0269-7491(00)00043-9), 2000.

Emberson, L. D., Pleijel, H., Ainsworth, E. A., van den Berg, M., Ren, W., Osborne, S., Mills, G., Pandey, D., Dentener, F., Büker, P., Ewert, F., Koeble, R., and Van Dingenen, R.: Ozone effects on crops and consideration in crop models, *European Journal of Agronomy*, Elsevier, 100(May), 19–34, <https://doi.org/10.1016/j.eja.2018.06.002>, 2018.

Ewert, F., and Porter, J. R.: Ozone effects on wheat in relation to CO<sub>2</sub>: Modelling short-term and long-term responses of leaf photosynthesis and leaf duration, *Global Change Biology*, 6(7), 735–750, <https://doi.org/10.1046/j.1365-2486.2000.00351.x>, 2000.

Farage, P. K., Long, S. P., Lechner, E. G., and Baker, N. R.: The sequence of change within the photosynthetic apparatus of wheat following short-term exposure to ozone, *Plant Physiology*, 95(2), 529–535, <https://doi.org/10.1104/pp.95.2.529>, 1991.

Farquhar, G. D., von Caemmerer, S., and Berry, J. A.: A biochemical model of photosynthetic CO<sub>2</sub> assimilation in leaves of C<sub>3</sub> species, *Planta*, 149, 78–90, <https://doi.org/10.1007/BF00386231>, 1980.

Feng, Y., Nguyen, T. H., Alam, M. S., Emberson, L., Gaiser, T., Ewert, F., and Frei, M.: Identifying and modelling key physiological traits that confer tolerance or sensitivity to ozone in winter wheat, *Environmental Pollution*, Elsevier Ltd, 304(April), 119251, <https://doi.org/10.1016/j.envpol.2022.119251>, 2022.

Feng, Y., Alam, M. S., Yan, F., Frei, M.: Alteration of carbon and nitrogen allocation in winter wheat under elevated ozone, *Plant Science*, Elsevier, 338, 111924, <https://doi.org/10.1016/j.plantsci.2023.111924>, 2024.

Feng, Z., Pang, J., Kobayashi, K., Zhu, J., OTR, R.D.: Differential responses in two varieties of winter wheat to elevated ozone concentration under fully open-air field conditions, *Global Change Biology*, 17(1), 580–591, <https://doi.org/10.1111/j.1365-2486.2010.02184.x>, 2011.

Feng, Z., Tang, H., Uddling, J., Pleijel, H., Kobayashi, K., Zhu, J., Oue, H., Guo, W.: A stomatal ozone flux-response relationship to assess ozone-induced yield loss of winter wheat in subtropical China, *Environmental Pollution*, Elsevier Ltd, 164, 16–23, <https://doi.org/10.1016/j.envpol.2012.01.014>, 2012.

Feng, Z., Wang, L., Pleijel, H., Zhu, J., Kobayashi, K.: Differential effects of ozone on photosynthesis of winter wheat among cultivars depend on antioxidative enzymes rather than stomatal conductance, *The Science of the Total Environment*, 572, 404–411, <https://doi.org/10.1016/j.scitotenv.2016.08.083>, 2016.

Feng, Z., Uddling, J., Tang, H., Zhu, J., and Kobayashi, K.: Comparison of crop yield sensitivity to ozone between open-top chamber and free-air experiments, *Global Change Biology*, 24(6), 2231–2238, <https://doi.org/10.1111/gcb.14077>, 2018.

Feng, Z., Agathokleous, E., Yue, X., Oksanen, E., Paoletti, E., Sase, H., Gandin, A., Koike, T., Calatayud, V., Yuan, X., Liu, X., De Marco, A., Jolivet, Y., Kontunen-Soppela, S., Hoshika, Y., Saji, H., Li, P., Li, Z., Watanabe, M., & Kobayashi, K.: *Emerging challenges of ozone impacts on Asian plants: Actions are needed to protect ecosystem health*. *Ecosystem Health and Sustainability*, 7(1), 1911602. <https://doi.org/10.1080/20964129.2021.1911602>, 2021.

Feng, Z., Xu, Y., Kobayashi, K., Dai, L., Zhang, T., Agathokleous, E., Calatayud, V., Paoletti, E., Mukherjee, A., Agrawal, M., Park, R. J., Oak, Y. J., and Yue, X.: *Ozone pollution threatens the production of major staple crops in East Asia*, *Nature Food*, 3, 47–56, <https://doi.org/10.1038/s43016-021-00422-6>, 2022..

Feng, Y., Nguyen, T. H., Alam, M. S., Emberson, L., Gaiser, T., Ewert, F., and Frei, M.: Identifying and modelling key physiological traits that confer tolerance or sensitivity to ozone in winter wheat, *Environmental Pollution*, 304, 119251, <https://doi.org/10.1016/j.envpol.2022.119251>, 2022.

Gelang, J., Pleijel, H., Sild, E., Danielsson, H., Younis, S., Selldén, G., and Wallin, G.: Rate and duration of grain filling in relation to flag leaf senescence and grain yield in spring wheat (*Triticum aestivum*) exposed to different concentrations of ozone, *Physiologia Plantarum*, 110(3), 366–375, <https://doi.org/10.1111/j.1399-3054.2000.1100311.x>, 2000.

Graham, A., Pope, R., Pringle, K., Arnold, S., Chipperfield, M., Conibear, L., Butt, E., Kiely, L., Knote, C., and McQuaid, J.: Impact on air quality and health due to the Saddleworth Moor fire in northern England, *Environmental Research Letters*, 15(7), 074001, <https://doi.org/10.1088/1748-9326/ab8496>, 2020.

Graham, A., Pringle, K., Pope, R., Arnold, S., Conibear, L., Burns, H., Rigby, R., Borchers-Arriagada, N., Butt, E., Kiely, L., Reddington, C., Spracklen, D., Woodhouse, M., Knote, C., and McQuaid, J.: Impact of the 2019/2020 Australian Megafires on Air Quality and Health, *GeoHealth*, 5(10), e2021GH000454, <https://doi.org/10.1029/2021GH000454>, 2021.

Grandjean, A., and Fuhrer, J.: Growth and leaf senescence in spring wheat (*Triticum aestivum*) grown at different ozone concentrations in open-top field chambers, *Environmental Pollution*, 59, 299–314, 1989.

Guan, X., Song, L., Wang, T. C., Turner, N., and Li, F.: Effect of Drought on the Gas Exchange, Chlorophyll Fluorescence and Yield of Six Different-Era Spring Wheat Cultivars, *Journal of Agronomy and Crop Science*, 201(4), 253–266, <https://doi.org/10.1111/jac.12103>, 2015.

Guarin, J. R., Kassie, B., Mashaheet, A. M., Burkey, K., and Asseng, S.: Modeling the effects of tropospheric ozone on wheat growth and yield, *European Journal of Agronomy*, 105, 13–23, <https://doi.org/10.1016/j.eja.2019.03.001>, 2019.

Guarin, J. R., Jägermeyr, J., Ainsworth, E. A., Oliveira, F. A. A., Asseng, S., Boote, K., Elliott, J., Emberson, L., Foster, I., Hoogenboom, G., Kelly, D., Ruane, A. C., and Sharps, K.: Modeling the effects

of tropospheric ozone on the growth and yield of global staple crops with DSSAT v4.8.0, *Geoscientific Model Development*, 17, 2547–2567, <https://doi.org/10.5194/gmd-17-2547-2024>, 2024.

Herman, J., and Usher, W.: SALib: An open-source Python library for sensitivity analysis, *J. Open Source Softw.*, 2(9), <https://doi.org/10.21105/joss.00097>, 2017.

Huang, H., Huang, J., Li, X., Feng, J., Zhuo, W., Wu, Y., Niu, Q., Su, W., and Yin, Y.: A dataset of winter wheat aboveground biomass in China during 2007–2015 based on data assimilation, *Scientific Data*, Springer US, 9(1), 1–11, <https://doi.org/10.1038/s41597-022-01305-6>, 2022.

Hussain, A., and Bangash, R.: Impact of Climate Change on Crops' Productivity across Selected Agro-ecological Zones in Pakistan, *The Pakistan Development Review*, 56(2), 163–187, <https://www.jstor.org/stable/26875191>, 2017.

Jaggi, M., Ammann, C., Neftel, J., and Fuhrer, J.: Environmental control of profiles of ozone concentration in a grassland canopy, *Atmospheric Environment*, 40(28), 5496–5507, <https://doi.org/10.1016/j.atmosenv.2006.01.025>, 2006.

Jones, H. G.: *Plants and microclimate: A quantitative approach to environmental plant physiology*, Cambridge University Press, 1992.

Kohut, R. J., Amundson, R. G., Laurence, J. A., Colavito, L., van Leuken, P., and King, P.: Effects of Ozone and Sulfur Dioxide on Yield of Winter Wheat, *Phytopathology*, 77, 71–74, <https://doi.org/10.1094/Phyto-77-71>, 1987.

Konduri, V. S., Tomas, V. J., Ganguly, S., and Ganguly, A. R.: Data Science for Weather Impacts on Crop Yield, *Frontiers in Sustainable Food Systems*, 4(May), 52, <https://doi.org/10.3389/fsufs.2020.00052>, 2020.

Lee, J. D., Drysdale, W. S., Finch, D. P., Wilde, S. E., and Palmer, P. I.: UK surface NO<sub>2</sub> levels dropped by 42% during the COVID-19 lockdown: Impact on surface O<sub>3</sub>, *Atmospheric Chemistry and Physics*, 20(24), 15743–15759, <https://doi.org/10.5194/acp-20-15743-2020>, 2020.

Leung, F., Williams, K. E., Sitch, S., Tai, A. P. K., Wiltshire, A., Gornall, J., Ainsworth, E. A., Arkebauer, T., and Scoby, D.: Calibrating soybean parameters in JULES 5.0 from the US-Ne2/3 FLUXNET sites and the SoyFACE-O<sub>3</sub> experiment, *Geoscientific Model Development*, 13(12), 6201–6213, <https://doi.org/10.5194/gmd-13-6201-2020>, 2020.

IPCC: *Climate Change 2021: The Physical Science Basis. Contribution of Working Group I to the Sixth Assessment Report of the Intergovernmental Panel on Climate Change*, Cambridge University Press, <https://doi.org/10.1017/9781009157896>, 2021

Leuning, R.: Modeling stomatal behavior and photosynthesis of *Eucalyptus grandis*, *Australian Journal of Plant Physiology*, 17(2), 159–175, 1990.

Leuning, R.: A critical appraisal of combined stomatal models for C<sub>3</sub> plants, *Plant, Cell & Environment*, 18(4), 339–355, 1995. Available at: <http://www.unc.edu/courses/2010spring/geog/595/001/www/Leuning95b-PCE.pdf>.

Li, A., Zhou, Q., and Xu, Q.: Prospects for ozone pollution control in China: An epidemiological perspective, *Environmental Pollution*, 285, 117670, <https://doi.org/10.1016/j.envpol.2021.117670>, 2021.

Li, D., Shindell, D., Ding, D., Xiao, Lu., Zhang, L., and Zhang, Y.: Surface ozone impacts on major crop production in China from 2010 to 2017, *Atmospheric Chemistry and Physics*, 22(4), 2625–2638, <https://doi.org/10.5194/acp-22-2625-2022>, 2022.

Li, K., Jacob, D. J., Shen, L., Lu, X., De Smedt, I., and Liao, H.: Increases in surface ozone pollution in China from 2013 to 2019: anthropogenic and meteorological influences, *Atmospheric Chemistry and Physics*, 20(19), 11423–11433, <https://doi.org/10.5194/acp-20-11423-2020>, 2020.

Lin, M., Horowitz, L. W., Payton, R., Fiore, A. M., and Tonnesen, G.: US surface ozone trends and extremes from 1980 to 2014: Quantifying the roles of rising Asian emissions, domestic controls, wildfires, and climate, *Atmospheric Chemistry and Physics*, 17(4), 2943–2970, <https://doi.org/10.5194/acp-17-2943-2017>, 2017.

Lim, P. O., Kim, H. J., and Nam, H. G.: Leaf senescence, *Annu. Rev. Plant Biol.*, 58, 115–136, <https://doi.org/10.1146/annurev.arplant.57.032905.105316>, 2007.

Liu, S., Mo, X., Lin, Z., Xu, Y., Ji, J., Wen, G., and Richey, J.: Crop yield responses to climate change in the Huang-Huai-Hai Plain of China, *Agricultural Water Management*, 97(8), 1195–1209, <https://doi.org/10.1016/j.agwat.2010.03.012>, 2010.

Liu, Z., Doherty, R. M., Wild, O., O’Connor F. M., and Turnock, T. S.: Tropospheric ozone changes and ozone sensitivity from the present day to the future under shared socio-economic pathways, *Atmospheric Chemistry and Physics*, 22(2), 1209–1227, <https://doi.org/10.5194/acp-22-1209-2022>, 2022.

Malhi, G. S., Kaur, M., and Kaushik, P.: Impact of Climate Change on Agriculture and Its Mitigation Strategies: A Review, *Sustainability*, 13(3), 1318, <https://doi.org/10.3390/su13031318>, 2021.

Mariën, B., Balzarolo, M., Dox, I., Leys, S., Marchand J. L., Géron, C., Portillo-Estrada, M., AbdElgawad, H., Asard, H., and Campioli, M.: Detecting the onset of autumn leaf senescence in deciduous forest trees of the temperate zone, *New Phytologist*, 224(1), 166–176, <https://doi.org/10.1111/nph.15991>, 2019.

Masutomi, Y.: The appropriate analytical solution for coupled leaf photosynthesis and stomatal conductance models for C3 plants, *Ecological Modelling*, 481, 110306, <https://doi.org/10.1016/j.ecolmodel.2023.110306>, 2023.

Medlyn, B. E., Dreyer, E., Ellsworth, D., Forstreuter, M., Harley, P., Kirschbaum, M., Roux, X., Montpied, P., Strassmeyer, J., Walcroft, A., Wang, K., and Loustau, D.: Temperature response of parameters of a biochemically based model of photosynthesis. II. A review of experimental data, *Plant, Cell and Environment*, 25(9), 1167–1179, <https://doi.org/10.1046/j.1365-3040.2002.00891.x>, 2002

Miller, J. D., Arteca, R. N., and Pell, E. J.: Senescence-Associated Gene Expression during Ozone-Induced Leaf Senescence in Arabidopsis, *Plant Physiology*, 120(4), 1015, <https://doi.org/10.1104/pp.120.4.1015>, 1999.

Muhie, S. H.: Novel approaches and practices to sustainable agriculture, *Journal of Agriculture and Food Research*, 10, 100446, <https://doi.org/10.1016/j.jafr.2022.100446>, 2022.

Mulvaney, M. J., and Devkota, P. J.: Adjusting Crop Yield to a Standard Moisture Content, EDIS, University of Florida George A Smathers Libraries, 2020(3), <https://doi.org/10.32473/edis-ag442-2020>, 2020.



Nguyen, T.H., Cappelli, G.A., Emberson, L., Ignacio, G.F., Irimescu, A., Francesco, S., Fabrizio, G., Booth, N., Boldeanu, G., Bermejo, V., Bland, S., Frei, M., Ewert, F., Gaiser, T.: Assessing the spatio-temporal tropospheric ozone and drought impacts on leaf growth and grain yield of wheat across Europe through crop modeling and remote sensing data. *European Journal of Agronomy* 153, 127052. <https://doi.org/10.1016/j.eja.2023.127052>, 2024.

LRTAP: Mapping critical levels for vegetation, chapter III of manual on methodologies and criteria for modelling and mapping critical loads and levels and air pollution effects, risks and trends, UNECE Convention on Long-range Transboundary Air Pollution, 2017

Van Oijen, M., and Ewert, F.: The effects of climatic variation in Europe on the yield response of spring wheat cv. Minaret to elevated CO<sub>2</sub> and O<sub>3</sub>: an analysis of open-top chamber experiments by means of two crop growth simulation models, *European Journal of Agronomy*, 10(3–4), 249–264, [https://doi.org/10.1016/s1161-0301\(99\)00014-3](https://doi.org/10.1016/s1161-0301(99)00014-3), 1999.

Osborne, S., Pandey, D., Mills, G., Hayes, F., Harmens, H., Gillies, D., Bücken, P., and Emberson, L.: New Insights into Leaf Physiological Responses to Ozone for Use in Crop Modelling, *Plants*, 8(4), 84, <https://doi.org/10.3390/plants8040084>, 2019.

Osborne, T., Gornall, J., Hooker, J., Williams, K. E., Wiltshire, A., Betts, R., and Wheeler, T.: JULES-crop: A Parametrisation of Crops in the Joint UK Land Environment Simulator, *Geoscientific Model Development*, 8(4), 1139–1155, <https://doi.org/10.5194/gmd-8-1139-2015>, 2015.

Pande, P., Hayes, F., Bland, S., Booth, N., Pleijel, H., and Emberson, L. D.: Ozone Dose-Response Relationships for Wheat Can Be Derived Using Photosynthetic-Based Stomatal Conductance Models, *Agricultural and Forest Meteorology*, 356, 110150, <https://doi.org/10.1016/j.agrformet.2024.110150>, 2024.

Pleijel, H., Danielsson, H., Emberson, L., Ashmore, M., and Mills, G.: Ozone Risk Assessment for Agricultural Crops in Europe: Further Development of Stomatal Flux and Flux–Response Relationships for European Wheat and Potato, *Atmospheric Environment*, 41(14), 3022–3040, <https://doi.org/10.1016/j.atmosenv.2006.12.002>, 2007.

Pury, D. G. G., and Farquhar, G. D.: Simple Scaling of Photosynthesis from Leaves to Canopies Without the Errors of Big-Leaf Models, *Functional Plant Biology*, 24(5), 537–557, <https://doi.org/10.1071/pp97030>, 1997.

Qin, X., Zhang, F., Liu, C., Yu, H., Cao, B., Tian, S., Liao, Y., and Siddique, K.: Wheat Yield Improvements in China: Past Trends and Future Directions, *Field Crops Research*, 177, 117–124, <https://doi.org/10.1016/j.fcr.2015.03.013>, 2015.

Schauberger, B., Rolinski, S., Schaphoff, S., and Müller, C.: Global Historical Soybean and Wheat Yield Loss Estimates from Ozone Pollution Considering Water and Temperature as Modifying Effects, *Agricultural and Forest Meteorology*, 265, 1–15, <https://doi.org/10.1016/j.agrformet.2018.11.004>, 2019.

Sharkey, T. D., Bernacchi, C. J., Farquhar, G. D., and Singaas, E. L.: Fitting Photosynthetic Carbon Dioxide Response Curves for C<sub>3</sub> Leaves, *Plant, Cell and Environment*, 30(9), 1035–1040, <https://doi.org/10.1111/j.1365-3040.2007.01710.x>, 2007.

Sillmann, J., Aunan, K., Emberson, L., Bücken, P., van Oort, B. V., O'Neill, C., Otero, N., Pandey, D., and Brisebois, A.: Combined Impacts of Climate and Air Pollution on Human Health and Agricultural

Productivity, *Environmental Research Letters*, 16(9), 074001, <https://doi.org/10.1088/1748-9326/ac1df8>, 2021.

Simpson, D., Benedictow, A., Berge, H., Bergström, R., Emberson, L. D., Fagerli, H., Flechard, C. R., Hayman, G., Gauss, M., Jonson, J. E., Jenkin, M. E., Nyíri, Á., Richter, C., Semeena, V. S., Tsyro, S., Tuovinen, J.-P., Valdebenito, Á., and Wind, P.: The EMEP MSC-W Chemical Transport Model – Technical Description, *Atmospheric Chemistry and Physics*, 12(16), 7825–7865, <https://doi.org/10.5194/acp-12-7825-2012>, 2012.

Yadav, D. S., Mishra, A. K., Rai, R., Chaudhary, N., Mukherjee, A., Agrawal, S. B., and Agrawal, M.: Responses of an Old and a Modern Indian Wheat Cultivar to Future O<sub>3</sub> Levels: Physiological, Yield and Grain Quality Parameters, *Environmental Pollution*, 263, 113939, <https://doi.org/10.1016/j.envpol.2020.113939>, 2020.

Sitch, S., Cox, P. M., Collins, W. J., and Huntingford, C.: Indirect Radiative Forcing of Climate Change Through Ozone Effects on the Land-Carbon Sink, *Nature*, 448(7155), 791–795, <https://doi.org/10.1038/nature06059>, 2007.

Tao, F., Feng, Z., Tang, H., Chen, Y., and Kobayashi, K.: Effects of Climate Change, CO<sub>2</sub> and O<sub>3</sub> on Wheat Productivity in Eastern China, Singly and in Combination, *Atmospheric Environment*, 153, 182–193, <https://doi.org/10.1016/j.atmosenv.2017.01.032>, 2017.

Thomson, A. M., Calvin, K. V., Smith, S. J., Kyle, G. P., Volke, A., Patel, P., Delgado-Arias, S. J., Bond-Lamberty, B., Wise, M., Clarke, L., and Edmonds, J.: RCP4.5: A Pathway for Stabilization of Radiative Forcing by 2100, *Climatic Change*, 109(1–2), 77–94, <https://doi.org/10.1007/s10584-011-0151-4>, 2011.

Triboi, E., and Triboi-Blondel, A. M.: Productivity and Grain or Seed Composition: A New Approach to an Old Problem - Invited Paper, *European Journal of Agronomy*, 16(3), 163–186, [https://doi.org/10.1016/S1161-0301\(01\)00146-0](https://doi.org/10.1016/S1161-0301(01)00146-0), 2002.

[Wallach, D.: Crop model calibration: A statistical perspective. \*Agronomy Journal\*, 103\(4\), 1141–1153. <https://doi.org/10.2134/agronj2010.0432>, 2011.](https://doi.org/10.2134/agronj2010.0432)

Wang, Q. J.: Using Genetic Algorithms to Optimise Model Parameters, *Environmental Modelling and Software*, 12(1), 27–34, [https://doi.org/10.1016/S1364-8152\(96\)00030-8](https://doi.org/10.1016/S1364-8152(96)00030-8), 1997.

Yang, L., Liu, S., Tsoka, S., and Papageorgiou, L. G.: Mathematical Programming for Piecewise Linear Regression Analysis, *Expert Systems with Applications*, 44, 156–167, <https://doi.org/10.1016/j.eswa.2015.08.034>, 2016.

Zhang, X., Xu, W., Zhang, G., Lin, W., Zhao, H., Ren, S., Zhou, G., Chen, J., & Xu, X. (2023). First long-term surface ozone variations at an agricultural site in the North China Plain: Evolution under changing meteorology and emissions. *Science of The Total Environment*, 860, 160520. <https://doi.org/10.1016/j.scitotenv.2022.160520>, 2023.

Zheng, B., Chenu, K., Doherty, A., and Chapman, S.: The APSIM-Wheat Module (7.5 R3008), APSIM Initiative, 44 pp, 2015. Available at: <https://www.apsim.info/documentation/model-documentation/crop-module-documentation/wheat/>.

Zhu, X., Feng, Z., Sun, T., Liu, X., Tang, H., Zhu, J., Guo, W., and Kobayashi, K.: Effects of Elevated Ozone Concentration on Yield of Four Chinese Cultivars of Winter Wheat Under Fully Open-Air Field

Conditions, *Global Change Biology*, 17(8), 2697–2706, <https://doi.org/10.1111/j.1365-2486.2011.02400.x>, 2011.:-

### Acknowledgments

We acknowledge the financial support of the Science and Technology Facilities Council (STFC) Research Grant (ST/V002481/1) for the "Pollution and Climate Smart Agriculture in China (PaCSAC)" project which supported initial development of the DO3SE-Crop model. Support from the Royal Society through the International Exchanges 2021 Cost Share (NSFC) grant (IEC\NSFC\211154) facilitated the UK-China collaboration to parameterise the DO3SE-Crop model within the project "Understanding the role of air pollution and climate on staple crop yields and nutrition in China". We also received support from STFC Research Grant (ST/Y005317/1) under the EO4AgroClimate programme for the project "Towards a digital twin of cropping systems based on ingestion of EO into process-based crop models" which helped refine the DO3SE-Crop model for a broader set of country applications.

[We would also like to thank the anonymous reviewers for their insightful comments and suggestions, which helped clarify and improve the quality of this manuscript.](#)